Geophysical Journal International

Geophys. J. Int. (2026) **246,** 1–18
https://doi.org/10.1093/gji/ggag266
Advance Access publication 2026 July 07
Research paper

On the origin of mid-mantle discontinuities beneath the Central Pacific as revealed by long-period SS and PP precursors

Steve A. B. Carr,[1] Tolulope Olugboji ,[1,2,3] Lauren Waszek,[4] Ziqi Zhang [5] and Nicholas C. Schmerr,[5]

[1] *Department of Earth and Environmental Sciences, University of Rochester, Rochester, NY 14627, USA. E-mail: scarr13@ur.rochester.edu*
[2] *Department of Electrical and Computer Engineering, University of Rochester, Rochester, NY 14627, USA*
[3] *Georgen Institute of Data Sciences and AI, University of Rochester, Rochester, NY 14627, USA*
[4] *Physical Sciences, James Cook University, Douglas, Queensland 4814, Australia*
[5] *Department of Geology, University of Maryland College Park, College Park, MD 20742, USA*

Accepted 2026 July 1. Received 2026 June 30; in original form 2026 January 27

SUMMARY

The origin of seismic discontinuities in the Earth's mid-mantle (∼700–1400 km) remains debated, with competing hypotheses attributing them to either partial melting due to water transport across the transition zone or compositional heterogeneities (subducted crust). Distinguishing between these scenarios has been hindered by the inability of standard imaging techniques to extract robustly the polarity of weak seismic reflections amidst noise and reverberations that contaminate mid-mantle reflections. Here, we introduce a novel signal processing framework that combines curvelet-based wavefield separation with extended multitaper deconvolution to resolve this polarity ambiguity. We validate this approach by applying it to a high-quality data set of SS and PP precursors beneath the Central Pacific. This application yields the robust detection of a discontinuity at approximately 800 km depth, characterized by a sharp positive shear velocity contrast ($\delta V_S \approx +4$-5%) and a negligible density contrast. The observed positive polarity precludes partial melt or thermal plumes as primary causal mechanisms. Instead, the high-velocity, neutral-density signature is consistent with a layer of stagnant, subducted oceanic crust in thermal equilibration with the ambient mantle. These results demonstrate the efficacy of the deconvolution framework and provide direct seismic evidence for compositional stratification in the mid-mantle, supporting geodynamic models where viscosity increases facilitate the long-term preservation of recycled lithosphere.

Key words: Composition and structure of the mantle; Body waves; Seismic discontinuities.

1 INTRODUCTION

Recent high-resolution seismic investigations have revealed that the mid-mantle (∼700–1400 km) displays significant multiscale heterogeneity, characterized by widespread scattering and localized discontinuities (B. Tauzin *et al.* 2010; B. Schmandt *et al.* 2014; Z. Liu *et al.* 2018; L. Waszek *et al.* 2018; W.D. Frazer & J. Park 2021; S.A. Carr *et al.* 2025). The physical origins of these features, however, remain debated, pointing to a range of potential underlying mechanisms. The two leading hypotheses—dehydration melting (D. Bercovici & S.-I. Karato 2003; S.-I. Karato *et al.* 2020) and basalt enrichment (H.L.M. Bentham & S. Rost 2014; L. Waszek *et al.* 2021)—present distinct models for the thermochemical state and the long-term evolution of the mantle. The dehydration model invokes active dynamic processes, suggesting that observed discontinuities are caused by layers of partial melt formed when water is released from hydrated minerals convecting out of the water-rich mantle transition zone (D. Bercovici & S.-I. Karato 2003). Conversely, the basalt-enrichment model attributes mid-mantle scatterers to ancient or present-day compositional heterogeneity, where accumulations of unmixed subducted crust create seismic contrasts that extend from the mantle transition zone (MTZ) into the topmost regions of the lower mantle (L. Waszek *et al.* 2018; B. Tauzin *et al.* 2022; M. Murakami *et al.* 2024). Additionally, recent work suggests that strong seismic anisotropy associated with mid-mantle deformation could also produce detectable discontinuities in this depth range (J. Wookey *et al.* 2002; Q. Huang *et al.* 2019).

The different hypotheses predict physically distinct seismic signatures (Fig. 1). Dehydration melting is predicted to produce a sharp reduction in shear velocity (V_s) with negligible density change, resulting in a negative seismic impedance contrast (D. Bercovici & S.-I. Karato 2003; T. Yoshino *et al.* 2007; S.-I. Karato *et al.* 2020). Prior observations and modelling of *Ps* converted waves suggest that dehydration melting produces shear velocity reductions of approximately 4% for layers above the 410-km discontinuity and 1.6–2.8% for those below the 660-km discontinuity (B. Schmandt *et al.* 2014; W.D. Frazer & J. Park 2021; S.A. Carr *et al.* 2025). These estimates

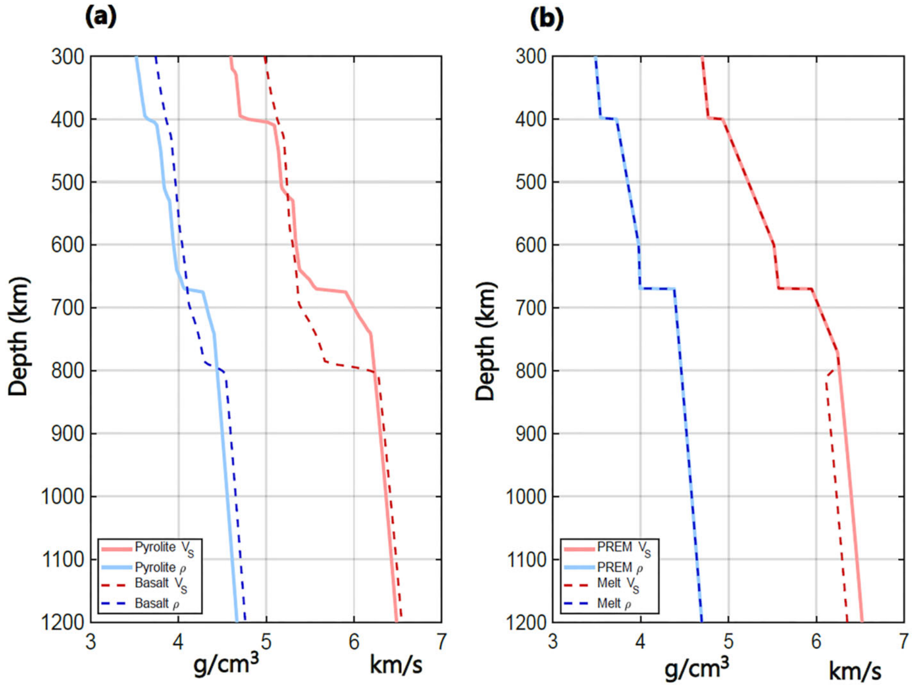

Figure 1. Seismic fingerprints of competing mid-mantle hypotheses. Comparison of the 1-D velocity (V_S) and density (ρ) profiles for the two competing hypotheses. (a) The Compositional Model (Basalt Enrichment). (b) The Thermal/Volatile Model (Dehydration Melt) parametrized as a sharp velocity reduction atop the lower mantle.

however are derived from the immediate vicinity of the transition zone boundaries and may not directly scale to melt anomalies in the deeper mid-mantle. The seismic signature of basaltic enrichment is considerably more complex, as the polarity of the velocity contrast varies depending on the mineralogical setting (W. Xu *et al.* 2008). Mineral physics calculations predict that increased basalt fractions associated with garnet-rich assemblages generate a significant density increase (ρ) compared to a pyrolitic mantle (Fig. 1a; W. Xu *et al.* 2008; L. Stixrude & C. Lithgow-Bertelloni 2012; T. Ishii *et al.* 2022). Such sharp impedance contrasts imply that chemically distinct layers should be seismically detectable at both their upper and lower interfaces, theoretically yielding converted phases of opposite polarity (L. Waszek *et al.* 2018). Temperature effects can further complicate these contrasts (W. Xu *et al.* 2008; L. Stixrude & C. Lithgow-Bertelloni 2012; L. Waszek *et al.* 2021). Therefore, robust constraints on the depth, amplitude and specifically the polarity of discontinuities offer a diagnostic tool to discriminate between volatile-induced melting and compositional heterogeneity.

Receiver functions, *P*-to-*S* converted waves, have displayed success for mapping velocity gradients in the mid-mantle (W.D. Frazer & J. Park 2021; S.A. Carr *et al.* 2025). However, their resultant seismic characteristics are inherently non-unique, since both partial melt and basaltic enrichment can manifest as similar velocity anomalies without a clear density constraint (W. Xu *et al.* 2008; B. Schmandt *et al.* 2014). Reflections from the underside of velocity contrasts (SS and PP precursors) offer a complementary probe. Reflection coefficients depend on both velocity and density, meaning underside reflections are sensitive to density contrasts that are invisible to methods sensitive primarily to velocity alone. As Fig. 1(a) demonstrates, this density contrast apparent only for basalt enrichment and not melt provides a key route to distinguish between formative models.

Despite this potential, previous global surveys using underside reflections have struggled to resolve these features robustly (L. Waszek *et al.* 2018, 2021; B. Tauzin *et al.* 2022). A primary limitation of prior work is the reliance on time-domain waveform stacking. This approach retains the information from the complex teleseismic source wavelets, which often include high-amplitude side-lobes (J. Park 2000; F. Bissig *et al.* 2022; W.D. Frazer & J. Park 2023). These side-lobes can obscure the true polarity of a reflection or, more critically, mimic a polarity reversal. This observational ambiguity makes it difficult to distinguish a true geophysical discontinuity from a source artifact, stalling efforts to discriminate between causal mechanisms.

To overcome these limitations, we introduce a signal processing framework designed to resolve the polarity ambiguity of previous global compilations. We combine two advanced techniques: curvelet-based wavefield separation (E. Candes *et al.* 2006; C. Yu *et al.* 2017; S. Goes *et al.* 2022) and extended multitaper spectral deconvolution (G. Helffrich 2006; W.D. Frazer & J. Park 2023). The former suppresses interfering phases while the latter removes source complexities to recover the true reflection polarity. This approach therefore implements a rigorous test on the origin of the mid-mantle discontinuities. We validate our framework using synthetic waveforms derived from mineral physics constraints, then apply it to a high-quality data set from the Central Pacific for proof-of-concept confirmation. By separating source effects from mantle structure in a methodological manner, we provide new insight into the underlying origin of mid-mantle discontinuities as accumulated subducted crust or volatile-induced melting.

2 PHYSICAL MODELLING AND SYNTHETIC DATA GENERATION

To predict the distinct seismic signatures of the two competing hypotheses, we first construct 1-D velocity and density profiles derived from petrological and mineral physics constraints (e.g. Fig. 1). These profiles serve as input for global wavefield simulations, allowing us to establish the expected polarity and amplitude response (i.e. the seismic fingerprints) for Basalt Enrichment versus Dehydration Melting.

2.1 Construction of 1-D thermochemical models

We model the 'Basalt Enrichment' scenario by generating phase assemblages and physical properties (V_S, V_P, ρ) using the Perple_X thermodynamic software (J.A. Connolly 2005). We consider three end-member bulk compositions: pyrolite (representing the ambient mantle), mid-ocean ridge basalt and harzburgite (representing depleted lithosphere). Bulk oxide compositions are adopted from W. Xu *et al.* (2008). Detailed phase proportions and sensitivity tests regarding thermal variations are provided in Figs S1 and S2 (Supplementary Material).

To simulate the aggregate seismic properties of a mantle containing accumulated oceanic crust, we compute mechanical mixtures of basalt and harzburgite using Voigt–Reuss–Hill averaging (D. Chung & W. Buessem 1968). We systematically explore the sensitivity of the seismic profile to basalt fraction (f_b) ranging from 0 to 100% in increments of 10%, as well as temperature variations (Figs S2 and S3, Supplementary Material). We observe that varying the basalt fraction significantly alters the depth and magnitude of mineral phase transitions; notably, a basalt enrichment of >20% is required to generate a sharp seismic discontinuity near 800 km depth that is distinct from the standard pyrolitic transition zone structure (see Fig. S3 in Supplementary Material). Based on this sensitivity analysis, and consistent with previous work (B. Tauzin *et al.* 2022), we select a representative model with 40% basalt enrichment calculated along a standard mantle adiabat ($T_p = 1600$ K) to serve as the input for the synthetic wavefield simulations.

For the 'Dehydration Melting' scenario, we parametrize the target discontinuity as a sharp low-velocity zone (LVZ) superimposed on the Preliminary Reference Earth Model (PREM; A.M. Dziewonski & D.L. Anderson 1981; Z. Liu *et al.* 2018). We parametrize this feature as a 2.6% step-function reduction in shear velocity (V_S) located below the 660-km discontinuity at ∼800 km. This is informed by previous constraints from high-resolution receiver function studies of mid-mantle LVZs (B. Schmandt *et al.* 2014; W.D. Frazer & J. Park 2021; S.A. Carr *et al.* 2025). We model the anomaly as a half-space since the simulated wavelengths resolve strictly the upper interface. While recent mineral physics constraints indicate that pure silicate melts at mid-mantle conditions can be highly dense (H. Fei 2021; O.T. Lord 2022), small melt fractions (∼1%) significantly reduce elastic moduli without appreciably altering the bulk density of the solid-melt aggregate (S.-I. Karato 2014). As a result, we keep the density profile fixed to the PREM reference (as illustrated in Fig. 1b).

2.2 Synthetic wavefield simulation

The 1-D thermochemical models described above serve as inputs for AXISEM (Axially Symmetric Spectral Element Method), a spectral-element wave propagation simulation (T. Nissen-Meyer *et al.* 2011). The source–receiver geometry spans epicentral distances of 100° to 180°, capturing the optimal geometry for observing mid-mantle reflectors using SS and PP precursors (L. Waszek *et al.* 2021). The synthetic seismograms were rotated into the vertical (Z), radial (R) and transverse (T) components; using transverse for SS data and vertical for PP. The simulations were performed with a minimum period of 4s. We then filter the synthetic seismograms between 0.005 and 0.05 Hz to match the spectral content of our observed data set.

An example of the synthetic wavefield for each scenario is illustrated in Fig. 2. Each model predicts a distinct SS and PP response; for brevity, we show one of the pair here (see Figs 2e and f). In each case, a mid-mantle discontinuity produces an additional wave arrival prior to that from the 660-km discontinuity (compare Figs 2e and f to Figs 2a and b). Interfering waves superimposed on the wavefields are high-amplitude source- and receiver-side multiples, as well as core-interacting phases, which obscure the target mid-mantle arrivals. Our goal is to improve the extraction and detection of these target signals. Therefore, we compute N-th root vespagrams ($N = 3$) for the raw synthetic waveforms (Fig. 3). This nonlinear stacking enhances the detection of coherent energy, resulting in an image that highlights a critical observational challenge.

In the absence of advanced signal processing, interfering phases and side-lobes of the source wavelet make it difficult to distinguish the predictive signature of the competing models: opposing polarities within the PP and SS reflectivity (Figs 3c and d). Additional issues with noise, relative to weak reflection, further hinder definitive identification of the true polarity of the target phases (SdS or PdP). Therefore, we implement a signal processing framework designed specifically to remove the source-side and wave-field interference that obscure robust signal identification and interpretation.

3 METHODOLOGY: SIGNAL PROCESSING FRAMEWORK

Global detections of mid-mantle heterogeneity have relied predominantly on time-domain array-processing of the long-period SS wave-field (L. Waszek *et al.* 2018). However, as demonstrated in Section 2, the diagnostic signature of mid-mantle structure is a weak precursor arriving just prior to the high-amplitude transition zone phases, and obscured frequently by source-side complexity and wavefield

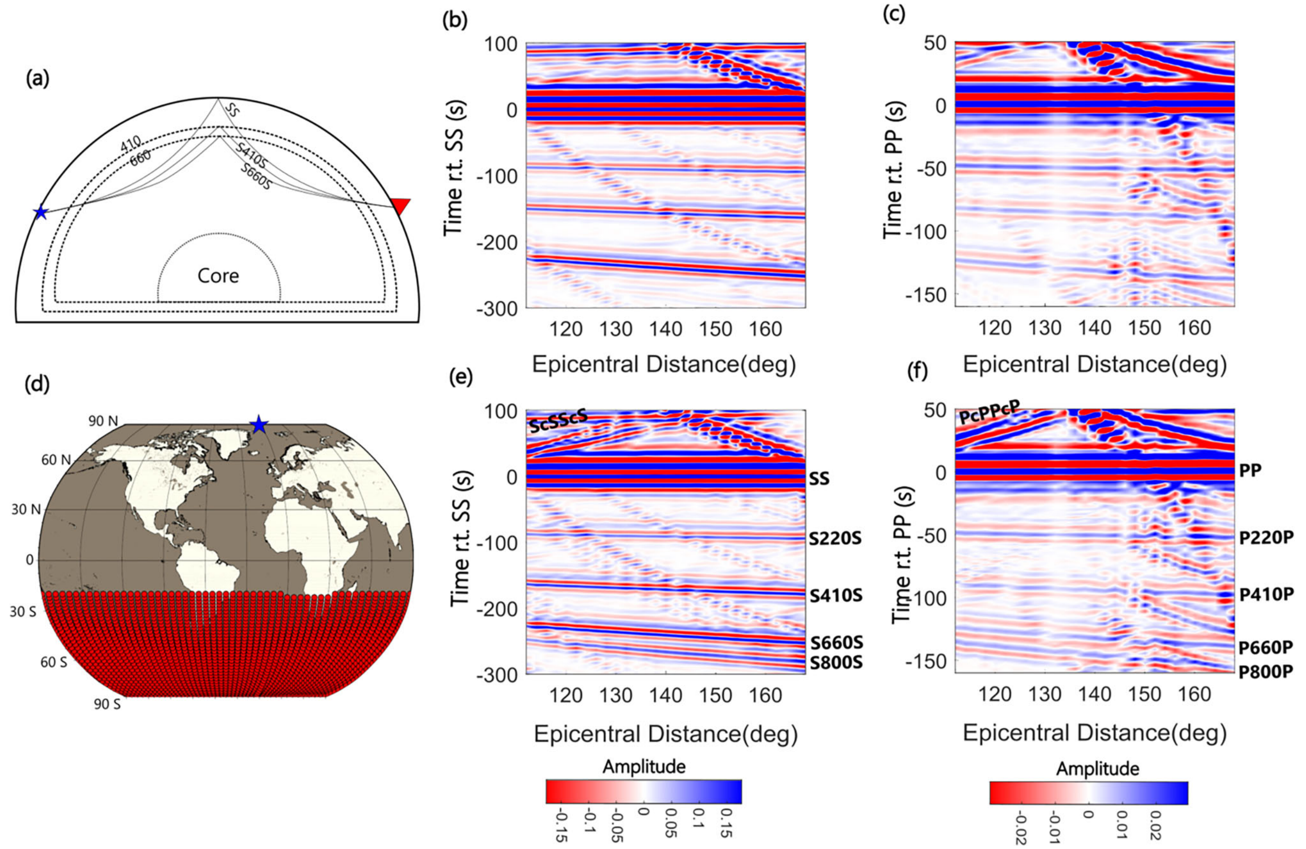

Figure 2. Raw wavefield simulations. (a) Ray path geometry for SS and PP underside reflections sampling mid-mantle discontinuities. (d) Simulation geometry showing the global distribution of the source (star) and receivers (circles) used in AXISEM. (b–c) Baseline raw synthetic seismograms calculated using a PREM model for transverse component SS (b) and vertical component PP (c). (e) Raw synthetic seismograms for the **Basalt Enrichment model** (SS component), generating a target discontinuity with a positive impedance contrast near 800 km depth. (f) Raw synthetic seismograms for the **Dehydration Melting model** (PP component), generating a target discontinuity with a negative impedance contrast. Note that across all models, the raw data are dominated by high-amplitude interference from multiply reflected phases, obscuring the target signals.

interference. Therefore, we isolate the diagnostic impedance signatures via a two-stage processing workflow: combining wavefield separation using the Curvelet Transform (E. Candes *et al.* 2006) with polarity recovery using the Extended Multitaper Spectral Deconvolution (G. Helffrich 2006; J. Park & V. Levin 2016). The curvelet transform and multitaper method (W.D. Frazer & J. Park 2023) have been used individually for transition-zone imaging (S. Goes 2002; C. Yu *et al.* 2017; W.D. Frazer & J. Park 2024), and here we integrate the algorithms into a unified workflow for joint SS-and PP-precursor imaging, providing a novel approach to mid-mantle exploration. These signal processing steps improve the detection and resolution of mid-mantle structure, especially in regions of complex interference and layering. Crucially, by recovering the true reflectivity, our approach provides accurate resolution of the robust amplitude and polarity constraints required to distinguish density-driven (compositional) anomalies from velocity driven (melting) anomalies (A. Deuss *et al.* 2006; A. Deuss 2009).

3.1 Wavefield separation with curvelet transform

The first goal of our workflow is to separate the weak mantle reflections from high-amplitude interfering phases. Three main classes of transform-based methods have been proposed to implement this: $f-k$ wavenumber filtering (H.-W. Zhou 2014), slowness stacks and invertible Radon transforms (Y.J. Gu & M. Sacchi 2009; Z. Zheng *et al.* 2015; T. Olugboji *et al.* 2023) and curvelet-based methods (C. Yu *et al.* 2017; J. Zhang & C.A. Langston 2020). Although $f-k$ and Radon transforms are effective for isolating linear features, they are global operators that can introduce smearing artifacts when phases exhibit curvature, or cross in the time-domain (S. Schneider *et al.* 2018). Furthermore, standard filtering becomes unstable when the teleseismic phases share similar frequency content or possess very similar slowness. To address this challenge, we employ the curvelet-based wavefield separation technique (Fig. 4). Unlike traditional filters that operate only on frequency (M. Naghizadeh 2012), the curvelet transform decomposes the seismic record section into a library of multiscale localized, directional wave packets (E. Candes *et al.* 2006). This 'locality' allows for the surgical removal of noise and interfering phases without the global smearing inherent to Radon or Fourier methods.

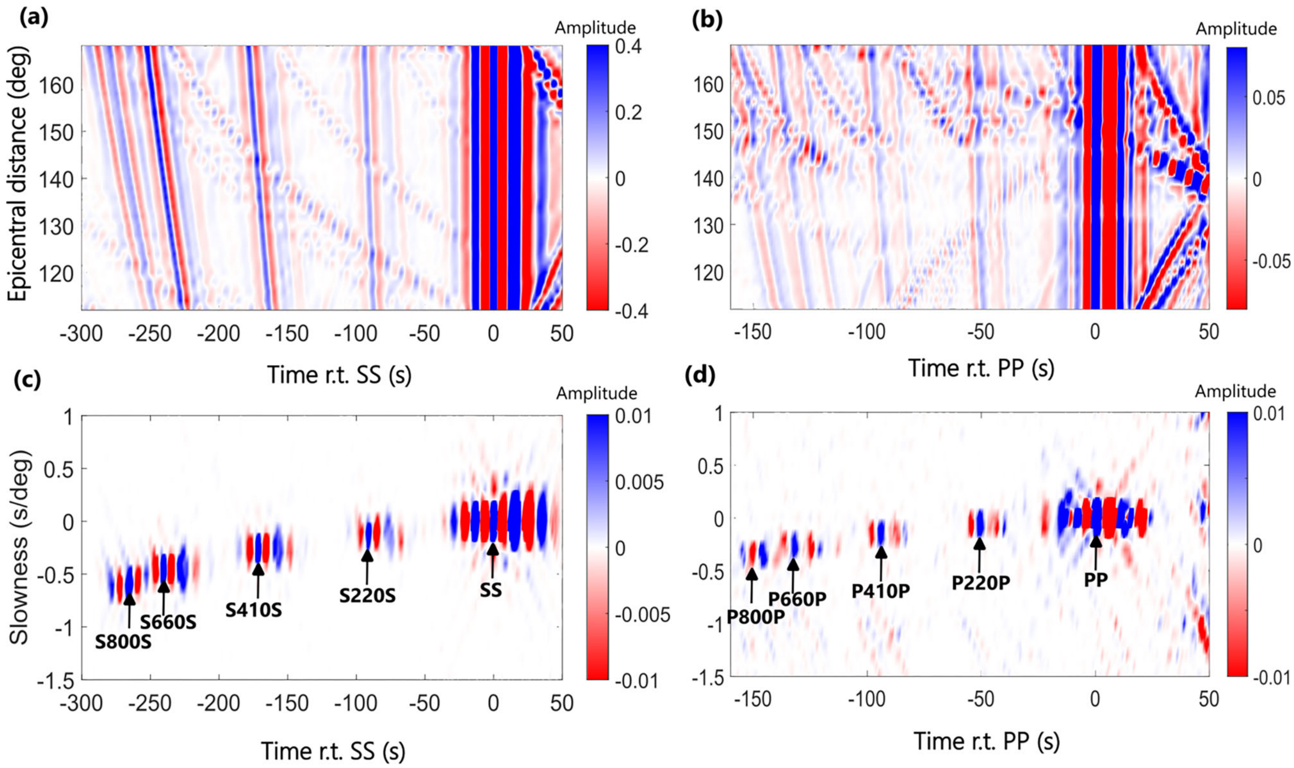

Figure 3. Vespagram analysis of raw seismic data. (a) Record section of undeconvolved SS synthetic data set (referenced from Fig. 2e). (b) Record section of undeconvolved PP synthetic data set (referenced from Fig. 2f). (c) *N*-th root vespagram of the SS data in panel (a), identifying key underside reflections. (d) *N*-th root vespagram of the PP data in panel (b), identifying corresponding *P*-wave reflections. Note the complexity of amplitudes and polarities prior to deconvolution.

We represent the seismic wavefield $u(x)$ as a linear combination of curvelet functions $\Psi_{s,\theta}$, each defined by a specific *scale s* (frequency band) and orientation θ (dip or slowness). The decomposition is computed via the inner product:

$$C_{s,\theta} = \int u(x)\Psi_{s,\theta}(x)\mathrm{d}x, \tag{1}$$

where $C_{s,\theta}$ are the curvelet coefficients representing the amplitude of coherent energy at that specific scale and dip (E. Candes *et al.* 2006). This sparse representation maps distinct seismic arrivals to different regions of the curvelet domain. For instance, reverberated phases (like ScS and PcP multiples) possess distinct moveout patterns and thus distinct orientations θ compared to the target SdS or PdP reflections.

To isolate the target signals, we apply a weighting mask $W_{s,\theta}$ guided by the predicted slowness of the interfering phases. This mask effectively mutes coefficients associated with the interfering phases while retaining the background signal. The 'clean' wavefield $\tilde{u}(x)$ is then reconstructed via the inverse transform:

$$\tilde{u}(x) = \sum_{s,\theta} W_{s,\theta} C_{s,\theta} \Psi_{s,\theta}(x). \tag{2}$$

This approach allows us to suppress high-amplitude reverberations while preserving the polarity and amplitude of the weak mid-mantle reflections, as demonstrated in previous applications to transition zone imaging (C. Yu *et al.* 2017, 2023).

3.2 Polarity recovery via spectral deconvolution

The second goal of our workflow, following application of curvelet filtering, is source-normalization through deconvolution. Though the curvelet-filtered seismograms are free from signal interference, they still contain side-lobes from the source wavelet that can mask the true polarity of a reflection. To enhance the true reflectivity, we apply the extended-time multitaper (ETMT) deconvolution method (G. Helffrich 2006; J. Park & V. Levin 2016). ETMT is a frequency-domain technique that uses a sequence of orthogonal Slepian tapers to stabilize the spectral division of the precursor trace (SdS or PdP) by the main phase (SS or PP). The Earth's reflectivity response $R(\omega)$ is then estimated by averaging the cross-spectrum of the precursor $P(\omega)$ and the source $S(\omega)$ over K orthogonal data tapers (W.D.

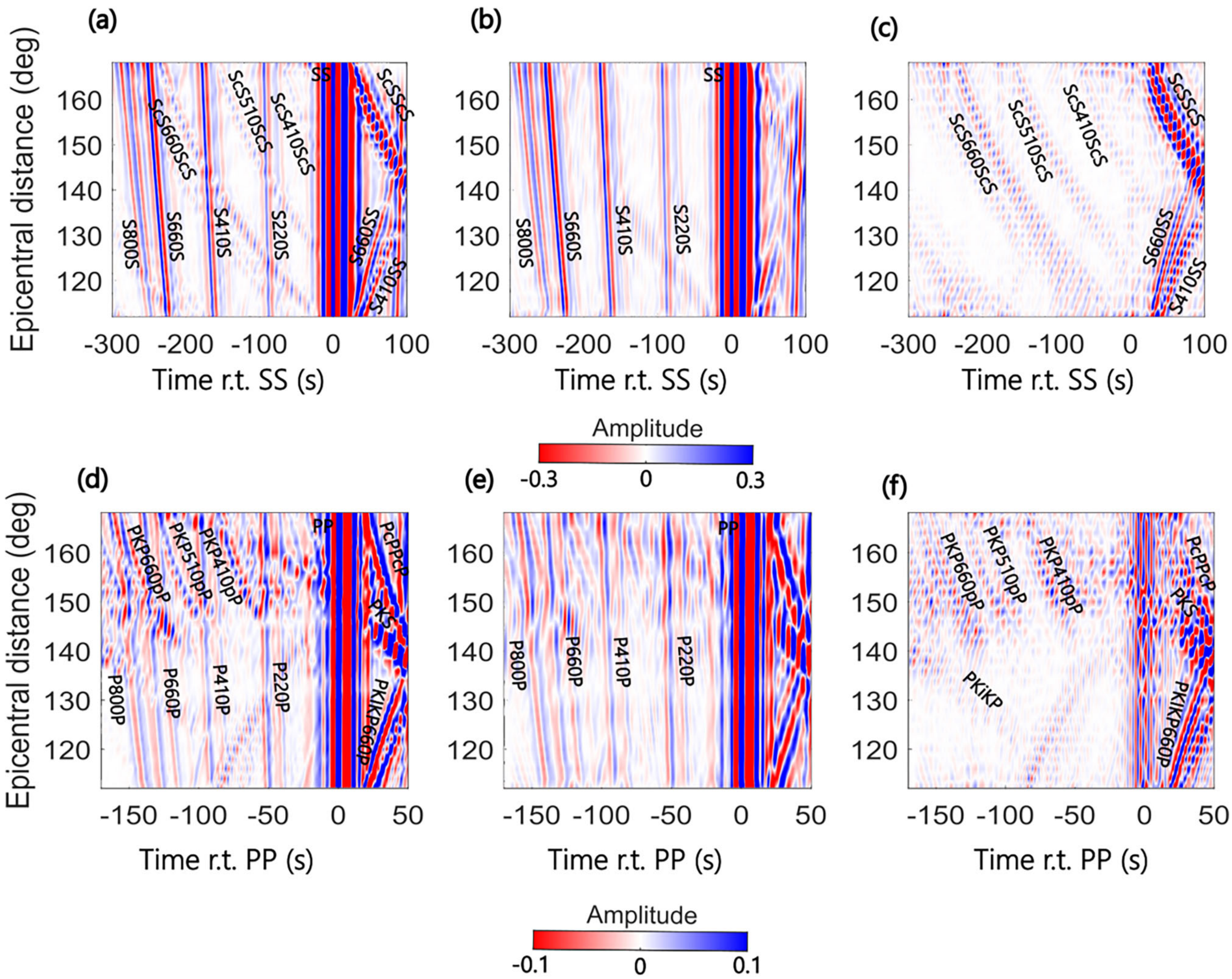

Figure 4. Wavefield separation using curvelet transform for (a–c) SS and (d–f) PP precursors. Left panels (a, d) show original synthetic seismograms containing both precursor signals and interfering phases. Middle panels (b, e) display the filtered wavefields after curvelet processing, highlighting the enhanced precursor arrivals. Right panels (c, f) show the removed residuals, dominated by interfering phases and noise suppressed during the separation process.

Frazer & J. Park 2023)

$$R(\omega) = \frac{\sum_{k=1}^{K} S_k^*(\omega) P_k(\omega)}{\sum_{k=1}^{K} |S_k(\omega)|^2 + S_0(\omega)}, \tag{3}$$

where $S_k(\omega)$ and $P_k(\omega)$ are the tapered spectra of the main phase and the precursor window, respectively, * denotes the complex conjugate and $S_0(\omega)$ is the squared multiple-taper estimate of the pre-event noise. Crucially, this term in the denominator stabilizes the spectral division, minimizing the instability caused by spectral holes in the source spectrum. By collapsing the source wavelet into a band-limited impulse response, this operation removes source-side complexity and allows for a robust reading of the discontinuity polarity (peak versus trough). We show, in Fig. 5, that applying ETMT on the curvelet-filtered seismograms, recovers robustly the true input polarity expected for each input model (compare Figs 5e and f with Figs 1a and b). Extended synthetic resolution tests confirm that deconvolution recovers the correct polarity of faint mid-mantle phases even in the presence of significant noise, and is stable across different high-frequency cut-offs (F_{cut})(Fig. S4, Supplementary Material). Furthermore, the standard moving window multitaper correlation, while comparable to the extended-time method, is harder to interpret (see Fig. S5 in Supplementary Material). The final vespagram on the deconvolved curvelet filtered seismogram is now free from the ambiguous or oscillatory signals that are present in standard time-domain linear stacking (compare Figs 5e and f with Figs 3c and d). With this new two-step signal processing framework in hand, we now turn to its application for distinguishing competing mid-mantle hypotheses with synthetic and real data sets.

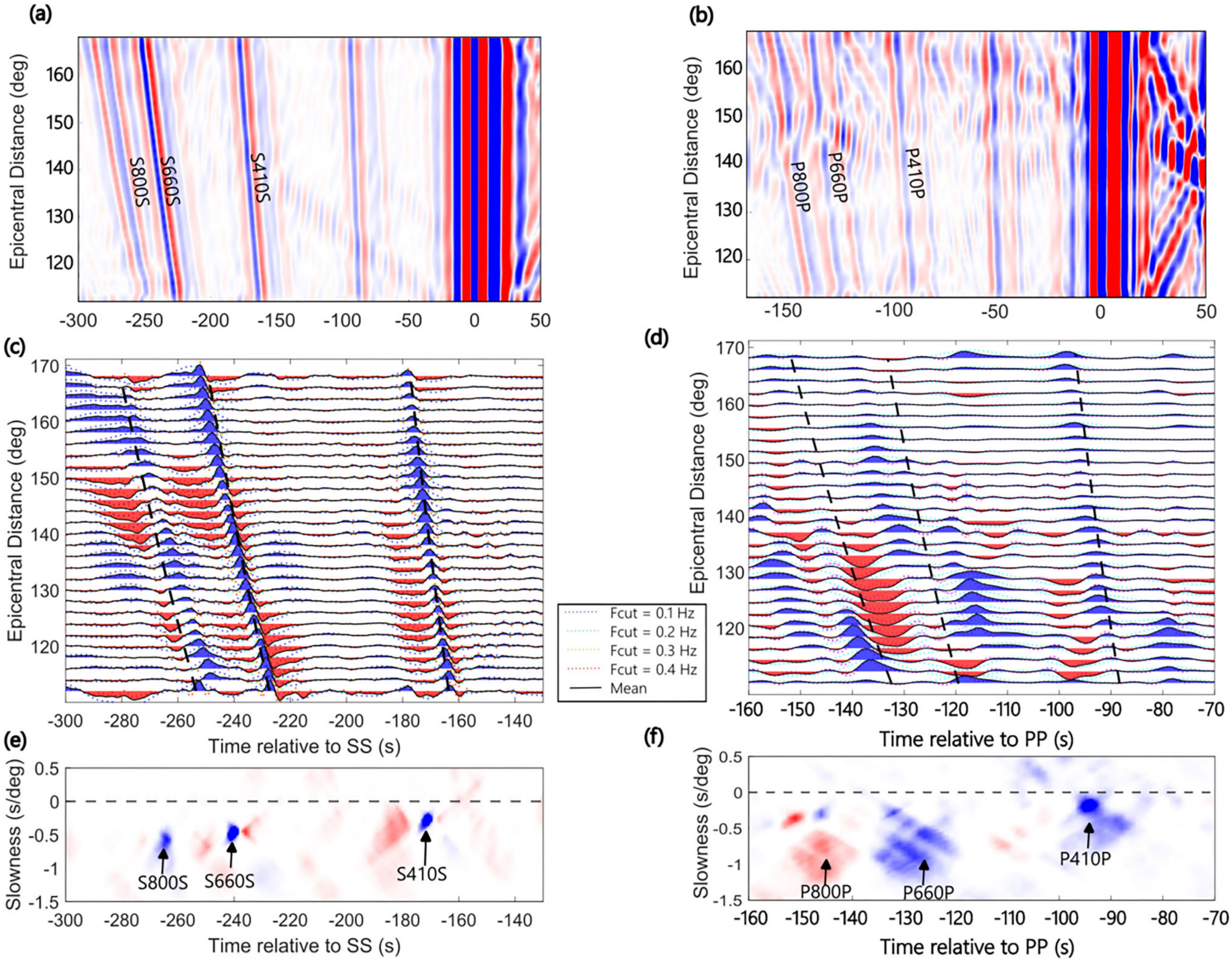

Figure 5. Extended multitaper deconvolution analysis on synthetics. (a, b) Record sections of the raw SS and PP input data prior to deconvolution. (c, d) Deconvolved receiver function gathers computed using the extended multitaper method (G. Helffrich 2006). Solid lines indicate the mean earth response, while coloured lines illustrate waveform stability across different frequency cut-offs (F_{cut}). (e, f) Vespagrams (slant stacks) of the deconvolved traces in panels (c) and (d).

4 RESULTS: SYNTHETIC SEISMIC FINGERPRINTS

4.1 Diagnostic fingerprints from filtered and deconvolved traces

The application of extended multitaper deconvolution to the filtered synthetic waveforms resolves the polarity ambiguity caused by source-side ringing. A comparison between the resulting source-normalized waveforms for the two end-member hypotheses reveals significantly improved interpretability (see Fig. 5). For the Basalt Enrichment model (illustrated here using the SS component, Fig. 5, left column), the deconvolved trace at the target depth range exhibits a robust positive amplitude anomaly (blue peak) relative to the reference phase. This positive polarity characteristic is consistent across the standard transition zone phases ($S_{410}S$, $S_{660}S$) and the target mid-mantle $S_{800}S$ phase. The robustness of these arrivals is visible in the vespagram (Fig. 5e), which shows clear, coherent stacking of positive polarity energy at ~ -270 s relative to SS (the complementary PP Basalt model is shown in Fig S7b in Supplementary Material).

In contrast, for the Dehydration Melting model (illustrated using the PP component, Fig. 5, right column), the deconvolved trace exhibits a distinct polarity reversal for the mid-mantle signal. While the standard 410 and 660 phases remain positive at ~ -95 and ~ -130 s, the signal corresponding to the mid-mantle low-velocity zone at ~ -150 appears as a negative polarity anomaly (red trough). We note that the distinct $P_{660}P$ phase visible here is a theoretical prediction of the 1-D PREM background model used in our simulations; in observational data, this phase is typically widely scattered or invisible due to low reflection coefficients (P.M. Shearer & M.P. Flanagan 1999). The deconvolved PP gathers exhibit slightly higher background noise levels relative to the SS data (compare Figs 5d and c), but the corresponding vespagram (Fig. 5f) demonstrates that the negative polarity signal stacks coherently despite increased scatter, and successfully distinguishes the physical impedance drop from incoherent noise (the complementary SS Melt model is shown in Fig. S7a in Supplementary Material). Our application of curvelet-filtering prior to deconvolution improves the coherence of the stacking, which is particularly crucial for clear detection of PdP arrivals (see Fig. S6 in Supplementary Material).

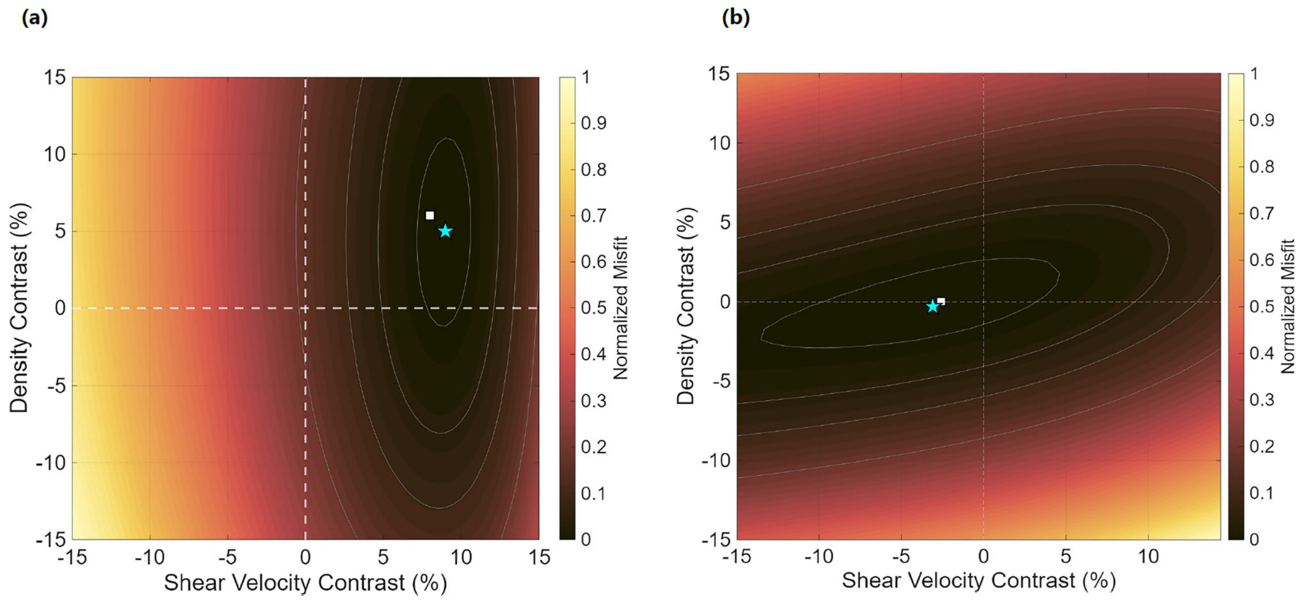

Figure 6. Synthetic recovery tests using joint grid search inversion. Normalized L2 misfit surfaces for (a) the Basalt Enrichment model and (b) the Dehydration Melting model. The square marks the true input parameters, and the star indicates the best-fit solution recovered by the joint inversion of SS and PP amplitudes. The joint inversion successfully constrains the solution into a well-defined minimum, allowing for the simultaneous recovery of both shear velocity and density contrasts.

4.2 Joint inversion for physical properties

Moving beyond qualitative polarity checks, we quantify the physical contrasts by performing a joint grid search inversion on the deconvolved amplitudes.The implementation follows a deterministic forward-modelling approach to solve for shear velocity (δV_S) and density ($\delta\rho$) contrasts. To avoid the amplitude distortion inherent to nonlinear signal processing, we extracted the absolute peak amplitudes using standard linear stacking ($N = 1$) from the stable gathers (e.g. Figs 5e and f) within a localized time-slowness window centered on the target mid-mantle depth. To map the solution space, we explored a 2-D grid ranging from -15 to $+15\%$, assuming a standard background mantle model (PREM) at 800 km depth. At each grid node, theoretical amplitudes were calculated using the PP and SS reflection coefficients for a solid–solid interface (K. Aki & P.G. Richards 2002). To accurately simulate partial melt during the forward modelling of the PP reflections, the compressional velocity contrast (δV_P) is scaled proportionately to δV_S to reflect a larger reduction, whereas a 1:1 ratio is maintained for the solid basalt model. The total misfit across the grid is defined as the sum of squared differences (L2 norm) between the observed and predicted reflection coefficients for both phases.

We validated this joint inversion scheme using our synthetic data sets (Fig. 6). For the **Basalt Enrichment** model, the inversion recovered a solution of $\delta V_S = +9.0\%$ and $\delta\rho = +5.0\%$ (True Input: $+8.0\%/+6.0\%$), which is an accurate characterization of the high-impedance, high-density nature of the anomaly. Conversely, for the **Dehydration Melting** model, the inversion recovered $\delta V_S = -3.1\%$ and $\delta\rho = -0.3\%$ (True Input: $-2.6\%/0.0\%$), successfully distinguishing the negative polarity melt signature from the basalt scenario. Crucially, while single-phase inversions typically exhibit elongated vertical valleys in the misfit surface due to the strong trade-off between density and velocity (see Fig. S8 in Supplementary Material) (P.M. Shearer & M.P. Flanagan 1999), the joint inversion is able to resolve this degeneracy. By combining constraints from SS and PP, the misfit contours converge into well-defined minima (Fig. 6), providing simultaneous recovery of both velocity and density contrasts with high fidelity.

While the joint inversion of SS and PP precursors theoretically minimizes parameter trade-offs, its practical application to real empirical data is limited. PP precursors typically exhibit significantly lower signal-to-noise ratios and suffer from greater phase interference, making them considerably more difficult to detect than their SS counterparts. Consequently, while we apply our full array-processing workflow to both SS and PP data sets to maximize detection potential, the lack of a robust, quantifiable PP signal ultimately restricts our empirical inversion to the SS data set in Section 5.4.

5 VALIDATION: APPLICATION TO PACIFIC DATA

We validate the discriminatory capability of our processing framework via a proof-of-concept application of the workflow to a large-scale data set from the Central Pacific. This region hosts two contrasting geodynamic regimes: the Hawaiian plume system, associated with strong thermal upwellings, juxtaposed with domains of seismically neutral or high-velocity mantle, potentially harbouring ancient stagnant subducted lithosphere (J. Ritsema *et al.* 2011; M.D. Ballmer *et al.* 2017; C. Cui *et al.* 2024). We analysed a high-quality data set of broad-band SS and PP waveforms with bounce points distributed across the Pacific basin (Fig. 7) in order to explore these areas. For

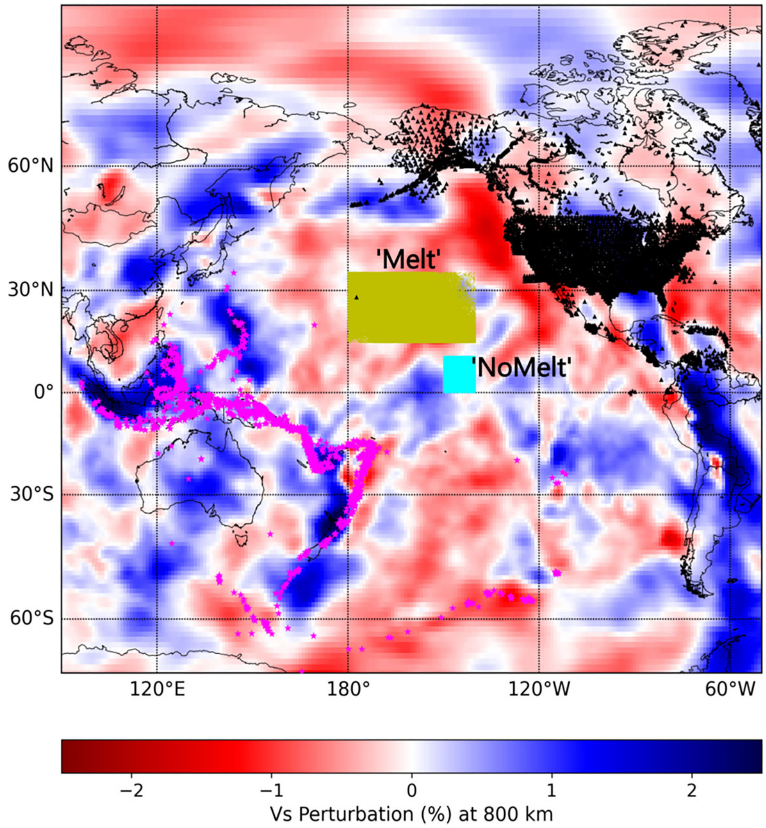

Figure 7. Study region. Underside reflection points (bounce points) are grouped by region: markers corresponding to the 'Melt' subset spatially correlate with the low-velocity anomalies associated with the Hawaiian plume system, while those corresponding to the 'NoMelt' background subset sample the surrounding relatively high-velocity or neutral mantle structure Earthquake locations are indicated by stars, and recording stations by triangles. Shear-wave velocity perturbations from the GLAD-M35 global adjoint tomography model (C. Cui *et al.* 2024) at 800 km depth are shown in the background.

comparative analysis, we defined two distinct subregions based on shear-wave velocity perturbations from the GLAD-M35 tomographic model (C. Cui *et al.* 2024). The first, designated as the 'Melt' region (indicated by yellow markers in Fig. 7), encapsulates the strong low-velocity anomalies surrounding the Hawaiian hotspot region; This zone serves as the primary test ground for the partial melting hypothesis, in which negative-polarity reflectors would be expected (Z. Zhang *et al.* 2023). Conversely, the 'NoMelt' control region (indicated by cyan markers) samples a spatially distinct reference zone, slightly south in the Pacific, characterized by high-velocity or neutral mantle structure. This acts as a critical control to test for the positive-polarity signatures expected from cold, chemically distinct material in the absence of plume influence.

The data set comprises over 100 000 SS and PP waveforms recorded by the USArray Transportable Array and Global Seismographic Network, with epicentral distances of 100°–180° to optimize the observation of wide-angle underside reflections. We select high-quality events with magnitudes $M \geq 6$ and apply the same pre-processing steps used for the synthetics (rotation to the radial–transverse–vertical system, and bandpass filtering between 0.005 and 0.05 Hz. Prior to processing, traces were aligned on the peak amplitude of the reference SS or PP phases to correct for traveltime variations. Finally, we apply curvelet-based wavefield separation to suppress the strong interference from the multiply reflected phases visible in the raw stacks (Fig. 8).

5.1 Application of wavefield separation to pacific data

We ensure that the spectral deconvolution operates on the primary Earth response rather than interfering artifacts by applying the curvelet-based wavefield separation workflow to the Pacific data set to isolate the target underside reflections from high-amplitude interference (Fig. 9). The residual wavefields (Figs 9a and b) contain the energy suppressed by the curvelet filter, consisting primarily of incoherent noise and high-amplitude multiples with move-out trends distinct from the target precursors. In contrast, the reconstructed wavefields (Figs 9 and d) preserve the coherent energy associated with the underside reflections.

The corresponding vespagrams of the filtered data (Figs 9e and f) confirm the robust recovery of global transition zone phases (e.g. $S_{660}S$, $S_{410}S$, $P_{410}P$) prior to deconvolution. Notably, the $P_{660}P$ phase is absent (Fig. 9f), consistent with its typically negligible amplitude in observational data sets. The wavefield is populated by a multitude of high-amplitude arrivals. This complexity arises because, while the curvelet filter effectively suppresses crossing phases based on slowness, it does not address the problem of the side-lobes. This means it is difficult to distinguish and validate true mid-mantle reflections from source-side artifacts without further processing.

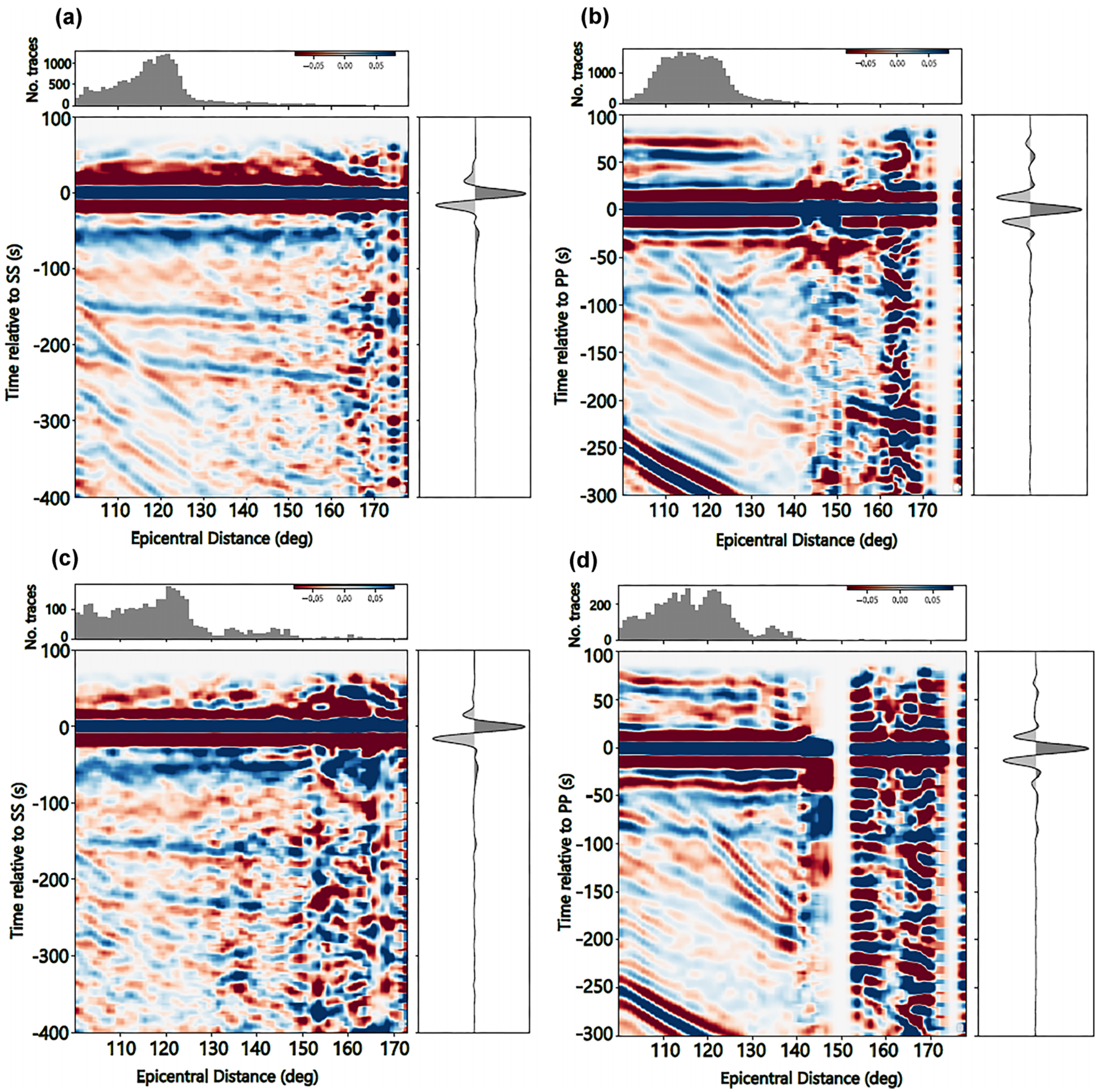

Figure 8. SS and PP record sections for the Pacific region (a, b) Raw SS and PP record sections for the hypothesized melt-present region. Top subplots display the number of traces per bin; right subplots show the corresponding stacked waveforms. (c, d) Raw SS and PP record sections for the NoMelt reference region.

5.2 Deconvolution results: Melt region

The application of Extended Multitaper (ETMT) deconvolution significantly improves image fidelity by suppressing artifacts and tightening the pulse widths. The raw SS and PP vespagrams (Figs 10a and b) are dominated by high-amplitude energy (strong positive and negative anomalies). However, the oscillatory nature of these raw signals makes it difficult to distinguish true mantle conversions from stacked side lobes and spectral leakage. As seen in the deconvolved vespagrams (Figs 10e and f), the 'smeared' high-amplitude patches converge into focused arrivals, reducing ambiguity and allowing for a more confident interpretation of the reflectivity structure.

In the deconvolved SS wavefield (Figs 10c and e), the global transition zone discontinuities ($S_{410}S$, $S_{660}S$) are recovered as coherent arrivals. We note that some localized amplitude variability at extreme epicentral distances in the individual gathers (e.g. negative amplitudes in Fig. 10c) is not a reflection of true structural complexity, but rather residual artifacts caused by imperfect wavefield separation and incoherent noise leaking into the deconvolution sidelobes. These local artifacts are effectively suppressed with slant stacking (Fig. 10e). Most notably, the deconvolution resolves a coherent arrival at a delay time of ~275 s before SS (corresponding to ~800 km depth). Unlike the ambiguous signals in the raw stack, this phase in the deconvolved data exhibits a relatively weak but stable

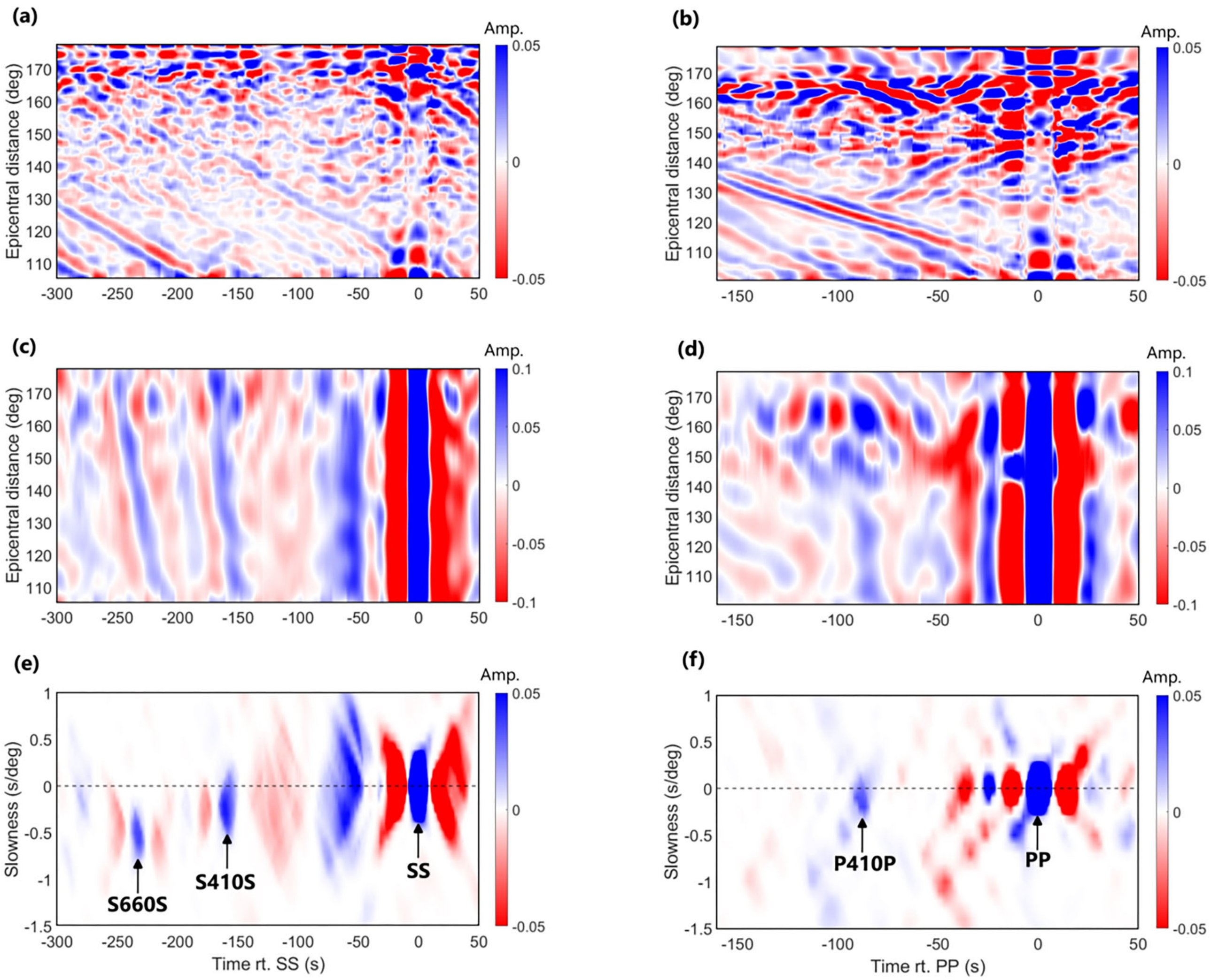

Figure 9. Signal separation of Pacific data sets. (a, b) Residual wavefields for representative SS and PP Pacific data sets, containing suppressed multiples and incoherent noise. (c, d) Reconstructed wavefields after curvelet filtering, isolating the primary underside reflection precursors. (e, f) Vespagrams of the filtered data in panels (c) and (d), confirming the visibility of key mantle phases (e.g. $S_{660}S$, $S_{410}S$, $P_{410}P$) prior to deconvolution.

positive polarity, confirming it as a distinct impedance boundary. Furthermore, a 2-D slowness grid search confirms that this signal originates from an in-plane structure, effectively ruling out out-of-plane scattering artifacts (see Fig. S10 in Supplementary Material).

In contrast, the PP results (Figs 10d and f) remain complex even after deconvolution. While the $P_{410}P$ is revealed as a sharp, coherent positive reflector at ~90 s, the deeper mantle structure is ambiguous. The $S_{660}S$ is clear, however the $P_{660}P$ phase is obscured, manifesting instead as an incoherent arrival near 600 km depth. In the individual gathers (Fig. 10d), reflectivity near 600–750 km appears discontinuous, with polarities that alternate or fade across epicentral distances. Consequently, these signals do not stack coherently in the vespagram (Fig. 10f), which lacks a definitive counterpart to the 660 or 800-km discontinuities observed in the SS data. Extended deconvolution tests before and after curvelet filtering show that this lack of detection is robust and only restricted to PP data (Fig. S9, Supplementary Material) (P.M. Shearer & M.P. Flanagan 1999; A. Deuss *et al.* 2006).

5.3 Deconvolution results: NoMelt region

We subsequently apply the same workflow to the 'NoMelt' reference region to establish a baseline for comparison for mid-mantle signals (Fig. 11). This region provides a control to determine whether the observed 800-km discontinuity is a localized anomaly or a more widespread feature. In the SS component (Figs 11c and e), the standard transition zone discontinuities are clearly imaged. The $S_{410}S$ phase is robust and coherent across all epicentral distances. The $S_{660}S$ is also visible, though it appears slightly more complex and less coherent. Crucially, a faint but coherent precursor is observed at a delay time consistent with the 800-km discontinuity (~ −275 s). A bootstrap resampling analysis further verifies that this faint precursor is statistically significant at the 95% confidence interval, ruling out a spurious alignment of background noise (see Fig. S11 in Supplementary Material). The PP component (Figs 11d and f) displays a highly coherent $P_{410}P$ phase, which serves as a benchmark for the quality of the *P*-wave data. However, as in the 'Melt' data

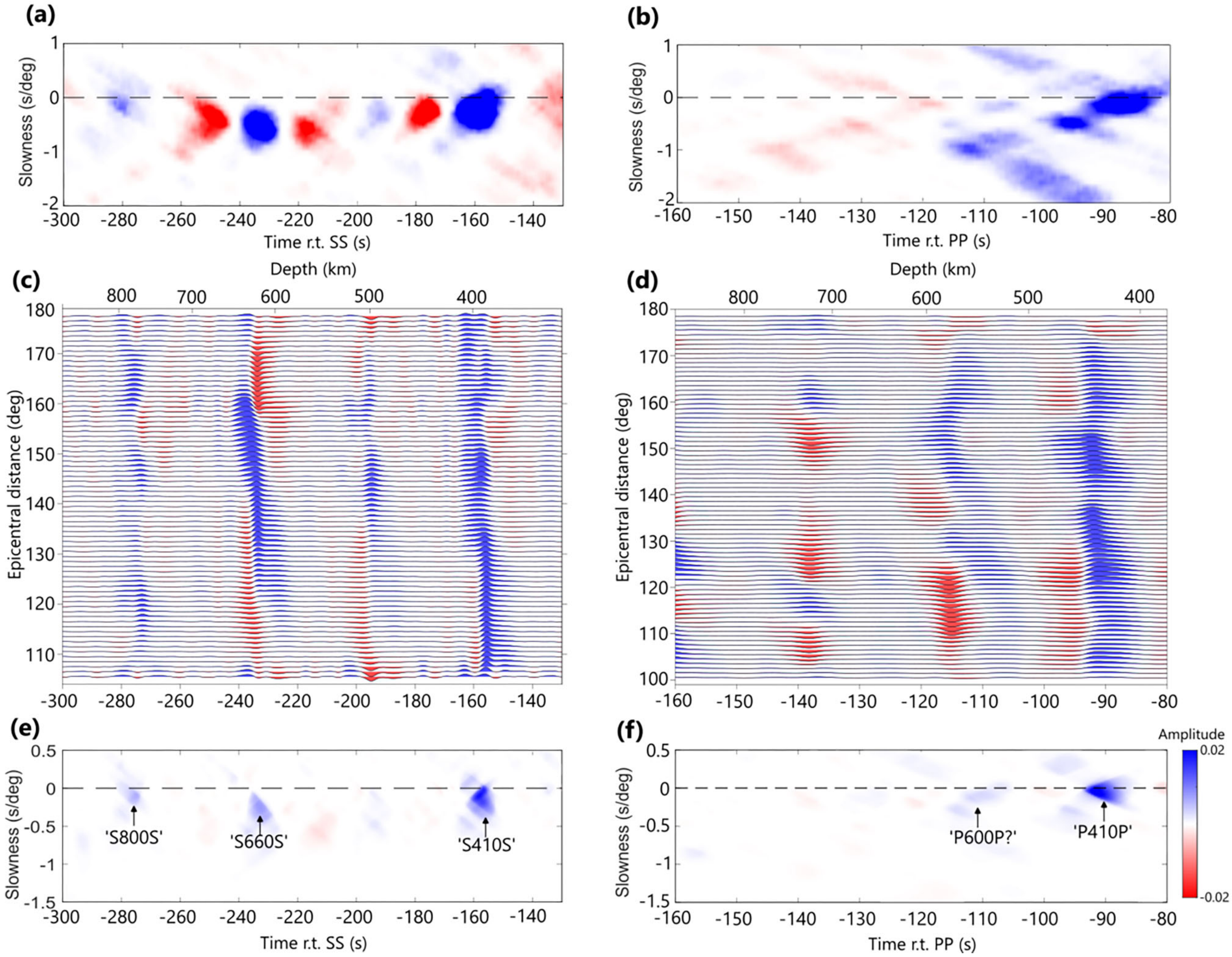

Figure 10. Deconvolution results for the melt-present region. (a, b) Vespagrams of the raw, undeconvolved SS and PP data. (c, d) Deconvolved gathers plotted against epicentral distance. Strong coherent arrivals are visible in the SS data (c), while the PP data (d) show greater complexity. (e, f) Vespagrams of the deconvolved gathers, revealing distinct phases. Note the robust recovery of '$S_{410}S$', '$S_{660}S$' and '$S_{800}S$' in the SS field, contrasted with the visibility of only '$P_{410}P$' and a possible '$P_{600}P$' in the PP field.

subset (directly underneath Hawai'i), the $P_{800}P$ signals from the deeper mid mantle are lacking. Although there is scattered energy in the 600–750 km depth range (labelled 'P600P?' in Fig. 11f), it lacks the pulse distinctness observed for the 410-km discontinuity.

5.4 Inversion of SS precursor amplitudes

Although our processing workflow was applied to both SS and PP data sets, we restrict the quantitative inversion to the SS precursors ($S_{800}S$). The absence of a mid-mantle compressional phase ($P_{800}P$) precludes the possibility of a joint SS–PP inversion. Consequently, we focus our constraints on the shear velocity and density contrasts derived from the SS data set. We perform a grid search inversion using the exact SS reflection coefficients for a solid–solid interface (K. Aki & P.G. Richards 2002) to quantify the physical contrasts associated with the detected 800-km discontinuity. To mitigate the effects of amplitude damping caused by regularization and stacking, rather than inverting the 800-km anomaly in isolation, we simultaneously invert the standard 660-km discontinuity extracted from the same time-slowness coordinates. This allows us to assess the strength of the 800-km target relative to a known global phase transition. Crucially, we explicitly employ standard linear stacking ($N = 1$) to extract absolute peak amplitudes for the quantitative inversion, while nonlinear stacking was utilized for robust phase detection and visualization. This ensures the extracted reflection coefficients preserve true amplitude fidelity before comparison with our forward models. Fig. S12 (Supplementary Material) uses a fully distance-dependent forward-modelled stack to show that variations in incidence angle do not bias the stacked amplitudes in our results. Fig. 12 presents the misfit surfaces for the 'Melt' and 'NoMelt' subsets from the SS data set.

For the melt data subset, the inversion recovers the 660-km reference signal with a strong positive shear velocity contrast ($\delta V_S = 8.0\%$) and density contrast ($\delta\rho = 7.5\%$). This high-amplitude reference is consistent with recent estimates for a basalt-enriched transition zone by C. Yu *et al.* (2023). Relative to this strong reference, the 800-km target is recovered with best-fit parameters comprising a positive velocity contrast of $\delta V_S = 4.0\%$, with a negligible density contrast of $\delta\rho = 0.5\%$. The shear velocity contrast ratio between

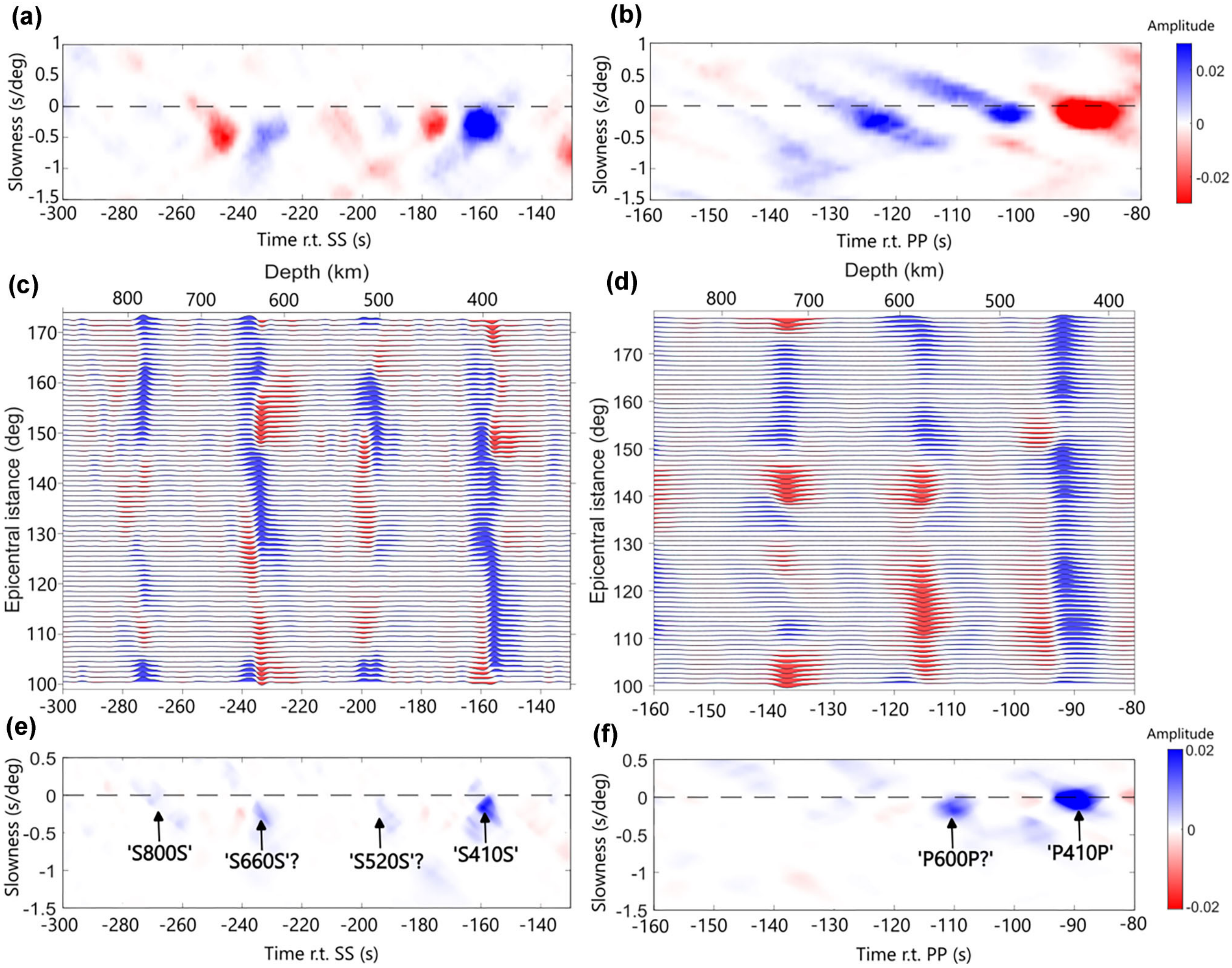

Figure 11. Deconvolution results for the NoMelt reference region. (a, b) Vespagrams of the raw, undeconvolved SS and PP data. (c, d) Deconvolved receiver function gathers plotted against epicentral distance. (e, f) Vespagrams of the deconvolved gathers.

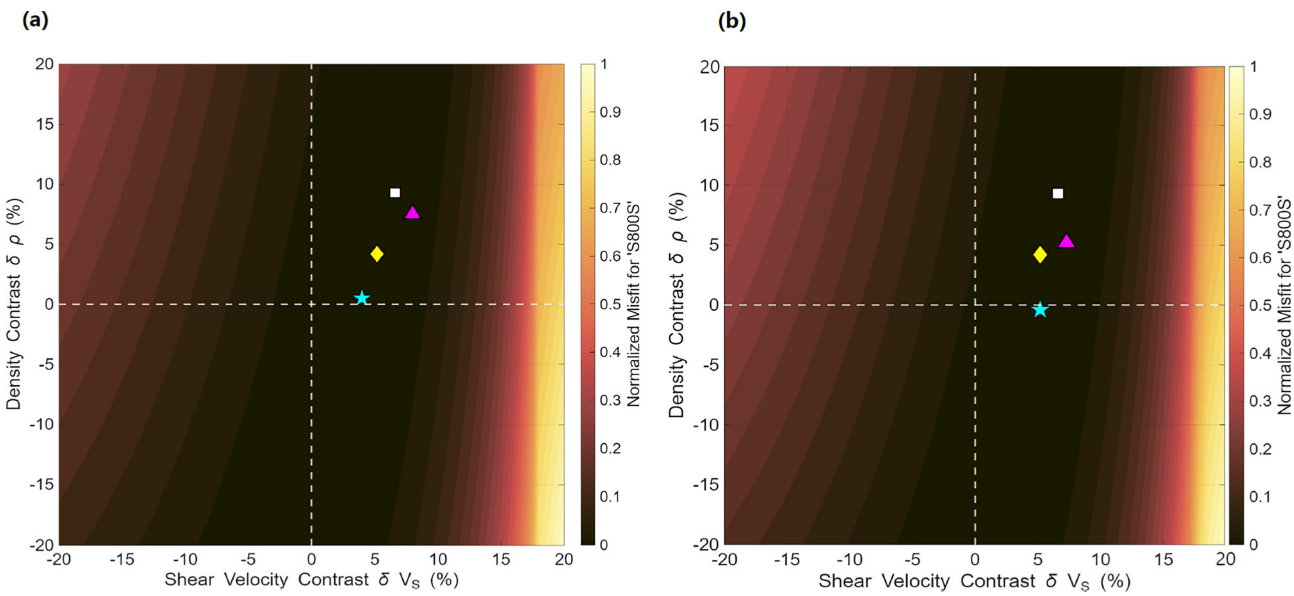

Figure 12. Grid search inversion of SS precursor amplitudes for regional subsets. Normalized L2 misfit surfaces for (a) the 'Melt' region subset and (b) the Background ('NoMelt') subset. The star marks the best-fit solution for the target 800-km discontinuity, while the triangle indicates the solution for the 660-km reference phase measured on the same traces. Reference markers include standard PREM values (square) and the basalt-enriched 660 estimate from C. Yu *et al.* (2023) (diamond). In both regions, the 660-km discontinuity is recovered with strong velocity and density contrasts and the 800-km target is robustly recovered as a high-velocity, density-neutral feature.

the target and reference ($\delta V_S^{800}/\delta V_S^{660}$) is $\sim$0.50. For the background 'NoMelt' data subset, the 660-km reference phase is recovered with $\delta V_S = 7.3\%$ and $\delta\rho = 5.2\%$. The 800-km target is again recovered as a distinct positive velocity contrast of $\delta V_S = 5.2\%$ with a near-zero density contrast ($\delta\rho = -0.4\%$). The shear velocity contrast ratio for this subset ($\delta V_S^{800}/\delta V_S^{660}$) is 0.71, indicating that the feature is present and seismically significant outside the anomalous melt region. In both data sets, the misfit surfaces exhibit elongation in the vertical axis, indicating that the shear velocity (δV_S) is well-constrained, but the density contrast ($\delta\rho$) is subject to significant trade-offs (Fig. 12). The density parameter remains less well constrained than shear velocity owing to the limited availability of high-quality PP precursor observations. However, two key physical properties are consistently resolved across both subsets: The shear velocity polarity, on average, is positive, and the density contrast is effectively neutral.

6 DISCUSSION

The difficulty in distinguishing low-amplitude, broad-band reflections from the sidelobes of the source wavelet and reverberating noise represents a significant hindrance in efforts to discriminate between compositional heterogeneities and melt-related anomalies in the mid-mantle. We demonstrate here that combining curvelet-based wavefield separation with ETMT deconvolution effectively resolves this 'polarity ambiguity'.

The positive polarity of the recovered 800-km velocity contrast is a critical discriminator for interpreting its physical origin. Recent imaging of the mid-mantle beneath the central Pacific has identified broad reflectors at $\sim$1000 km depth with negative polarity, which have been interpreted as the tops of thermochemical plumes or large-scale partial melt accumulations (Z. Zhang *et al.* 2023). However, the reverse time migration approach used by Z. Zhang *et al.* (2023) lacks explicit source-wavelet deconvolution, which may result in some ambiguity regarding the true polarity of the impedance contrast. In contrast, our observation of a sharp velocity increase aligns with previous detections of positive-impedance reflectors in the Pacific mid-mantle (Y. Shen *et al.* 2003). While Y. Shen *et al.* (2003) identified a sharp velocity increase near 1050 km beneath Hawaii, attributing it to a chemically distinct, potentially silicon-rich reservoir, they do not explicitly filter transition zone reverberations, which often contaminate *Ps* receiver functions in this depth window (J. Jenkins *et al.* 2017; S.A. Carr *et al.* 2025). In the absence of such filtering, multiples may be misidentified as structural features. Global surveys have also documented intermittent positive discontinuities between 800 and 1200 km depth (L. Waszek *et al.* 2018), particularly in our region of interest. These are often interspersed with negative polarity signals, and distinct from standard phase transitions. Our results support these observations and suggest a compositional origin, such as a chemically distinct layer (Y. Fukao & M. Obayashi 2013; M.D. Ballmer *et al.* 2015). Geodynamic simulations of mantle convection suggest that segregated basaltic crust can accumulate at the base of the transition zone and in the mid-mantle (T. Nakagawa *et al.* 2010; J. Yan *et al.* 2020), providing a robust mechanism for these positive velocity contrasts.

The detection of the 800-km feature in both the 'Melt' and 'NoMelt' background regions also challenges the constraint that mid-mantle heterogeneity is exclusively linked to active plume upwellings (J. Yan *et al.* 2020; J. Wang *et al.* 2024). The coherence of the 800-km phase over a broader region implies a laterally extensive stratification. This supports the 'marble cake' models of the mantle, in which ancient subducted crust is not immediately homogenized but survives as distinct lithologic layers (C.J. Allègre & D.L. Turcotte 1986; P.E. van Keken *et al.* 2002). A viscosity increase proposed near 1000 km depth (M.L. Rudolph *et al.* 2015) may act as a dynamical barrier, facilitating the stagnation of these crustal remnants (H. Marquardt & L. Miyagi 2015).

Perhaps the most enigmatic result of our inversion is the 'density paradox'. Despite the strong velocity contrast exhibited by the 800-km feature, its density contrast is negligible. This result suggests a physical state best described by 'neutral buoyancy'. In a purely thermal model, a cold stagnant slab should exhibit both high velocity and high density relative to the ambient mantle (S.P. Grand 2002; J. Ritsema *et al.* 2009). Although basalt is typically denser than the pyrolitic mantle in the transition zone, its density contrast varies with depth due to the differing compressibilities of lower-mantle mineral assemblages (bridgmanite and ferropericlase versus calcium silicate perovskite) (L. Stixrude & C. Lithgow-Bertelloni 2012; T. Ishii *et al.* 2022). Thus, our results suggest that the 800-km discontinuity may represent a layer of delaminated crust in thermal equilibration with the surrounding mantle, thereby retaining a high shear wave velocity (due to the high shear modulus of calcium perovskite) while settling into a depth of gravitational stability (B. Tauzin *et al.* 2022) (Fig. 13).

The interpretation of this feature is further complicated by the differences observed between the SS and PP wavefields. While the $S_{800}S$ phase is robustly detected, the corresponding ($P_{800}P$) phase is notably absent or below the noise level in our data set. The difficulty in observing *P*-wave precursors from the base of the transition zone is a historically documented challenge, often attributed to lower reflection coefficients relative to SS precursors (S. Lessing *et al.* 2015; F. Bissig *et al.* 2022). Consequently, the absence of a clear $P_{800}P$ signal likely stems from similar observational limitations rather than the feature being physically invisible to *P*-waves at the period of our data. However, even if a weak *P*-wave contrast exists, the high-velocity, neutral-density signature recovered from the inversion of the SS data set remains the most diagnostic characteristic. Future global studies utilizing larger, complementary data sets combined with advanced processing algorithms will improve insight into these mid-mantle features.

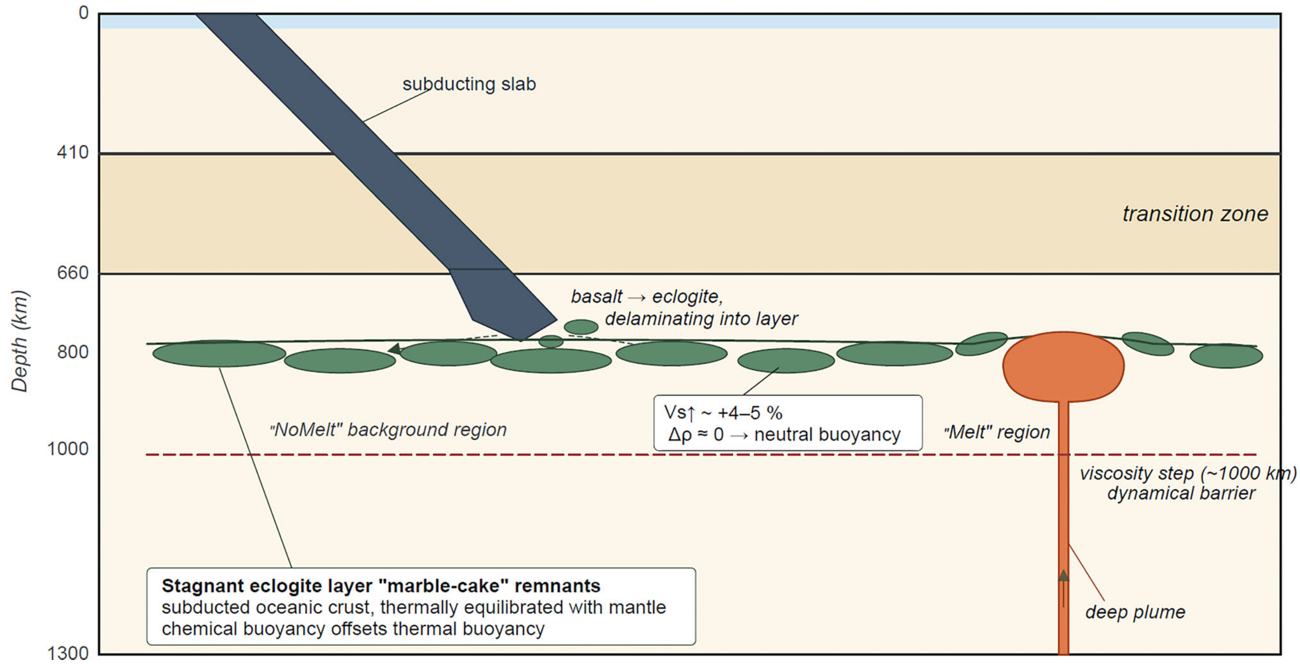

Figure 13. Conceptual schematic of mid-mantle stratification and the 'density paradox'. This synthesis illustrates the interpretation of the ~800 km discontinuity as a laterally extensive layer of stagnant, eclogitized oceanic crust accumulated near a viscosity barrier at 1000 km depth, thermally equilibrated with the ambient mantle such that chemical and thermal buoyancy approximately cancel. Subducting slab delivers basaltic crust which transforms to eclogite and accumulates as marble-cake remnants.

7 CONCLUSIONS

We present a robust detection of a mid-mantle seismic discontinuity at approximately 800 km depth beneath the Central Pacific, achieved through the application of a novel signal processing framework. By integrating curvelet-based wavefield separation with extended multitaper deconvolution, we successfully suppressed the interfering noise and source-side reverberations that have historically obscured the polarity of weak mid-mantle signals. This methodological advance allowed us to resolve the 'polarity ambiguity' inherent in previous global stacking studies and perform a quantitative inversion of the physical properties of the 800-km feature.

Our results reveal that the 800-km discontinuity is characterized by a sharp positive shear velocity contrast ($\delta V_S \approx +$4-5%) and a negligible density contrast. The unambiguous recovery of positive polarity across both the 'Melt' and background 'NoMelt' regions effectively rules out thermal plumes or widespread dehydration melting as the primary cause, as these mechanisms would generate negative impedance contrasts. Instead, the observed high-velocity, neutral-density signature is best explained by the presence of stagnant, subducted oceanic crust (eclogite) that has thermally equilibrated with the ambient mantle. In this scenario, the intrinsic chemical buoyancy of the basaltic crust offsets its thermal negative buoyancy, allowing it to settle at a depth of neutral stability.

These findings support a view of the mantle that is compositionally stratified, consistent with 'marble cake' and 'slab graveyard' models of mantle convection. The accumulation of ancient crust at mid-mantle depths implies that the viscosity increases near 1000 km depth may serve as a dynamical barrier to whole-mantle homogenization. Future applications of this deconvolution framework to global data sets will offer a clearer window into the fate of recycled lithosphere in the deep Earth.

ACKNOWLEDGMENTS

This work was made possible by the support from the National Science Foundation under grant number: 2339370. The authors acknowledge the use of the BlueHive Linux cluster at the University of Rochester's Center for Integrated Research Computing, CIRC (https://www.circ.rochester.edu/). The authors acknowledge many helpful discussions with Prof. Kevin Righter and the anonymous reviewers.

SUPPORTING INFORMATION

Supplementary data are available at *GJIRAS* online.

Figure S1. Calculated mineral phase proportions as a function of depth for the three end-member mantle compositions at a potential temperature of 1600 K: (a) Pyrolite, (b) Harzburgite and (c) Basalt. The variations in mineralogy illustrate the key phase transitions (e.g. olivine–wadsleyite–ringwoodite) that give rise to the seismic discontinuities in the transition zone.

Figure S2. Density and shear wave velocity profiles for pyrolite, harzburgite and basalt compositions. Profiles are computed for adiabatic geoterms with potential temperatures 1600, 1800, 2000 and 2200 K.

Figure S3. The effect of varying basalt fraction on (a) density and (b) *S*-wave velocity profiles. Each curve represents a different mechanical mixture of harzburgite and basalt, from 0% basalt (pure harzburgite) to 100% basalt.

Figure S4. Validation of the ETMT deconvolution algorithm using synthetic seismograms. The input traces were generated by convolving a Ricker wavelet with a known reflectivity series. (a) A noise-free synthetic trace. (b) The same synthetic trace contaminated with random noise. (c) Deconvolution result for the noise-free synthetic trace shown in panel (a). (d) Deconvolution result for the noisy trace shown in panel (b), demonstrating the robustness of the algorithm in recovering the original reflectivity spikes. 'Z' denotes the reference trace containing the primary phase (SS or PP) used as the source wavelet, and 'R' denotes the target trace containing the precursor arrivals.

Figure S5. Synthetic resolution test using standard Multi-Taper Correlation deconvolution (distinct from the ETMT method used in the main analysis). The input reflectivity model consists of positive velocity contrasts at 410 and 660 km, and a negative velocity contrast at 800 km. (a) Clean synthetic trace. (b) Synthetic trace with added random noise. (c, d) Recovered P410P/S410S pulse for clean and noisy data. (e, f) Recovered P660P/S660S pulse. (g, h) Recovered 800-km pulse, correctly resolving the negative polarity (trough). This confirms that the multitaper deconvolution framework robustly recovers negative polarities, supporting the interpretation that the positive 800-km phase observed in the real data is physical.

Figure S6. Assessment of noise suppression: ETMT deconvolution applied to non-curvelet filtered synthetic data sets. This figure serves as a direct comparison to Fig. 5 in the main text, illustrating the results when the curvelet denoising step is omitted. (a, c, e) Results for the SS Basalt data set: (a) raw unfiltered data, (c) deconvolved receiver function gather, (e) vespagram. (b, d, f). Results for the PP Melt data set: (b) raw unfiltered data, (d) deconvolved receiver function gather, and (f) vespagram. Compared to the clean signals in Fig. 5, these panels exhibit significantly higher noise levels and spurious phases caused by reverberations (multiples), demonstrating the necessity of the curvelet filtering step to isolate the precursor signals.

Figure S7. Processing of synthetic data sets for the complementary model phases required for the joint inversion. This figure parallels Fig. 5 in the main text but displays the alternative phase-model combinations: (a, c, e) SS precursors generated for the Dehydration Melting model. (b, d, f) PP precursors generated for the Basalt Enrichment model. The panels display the input data (a, b), the deconvolved receiver function gathers (c, d) and the final vespagrams (e, f). These data sets provided the necessary amplitudes to complete the joint inversion grid searches shown in Fig. 6.

Figure S8. Grid search inversion results using single seismic phases, illustrating the parameter trade-offs inherent in independent inversions. (a) SS-only inversion for the Basalt Enrichment model ($dV_S = +8\%$, $d_\rho = +6\%$). The low-misfit region forms a vertical valley, indicating that while shear velocity is well-recovered, density is poorly constrained. (b) PP-only inversion for the Dehydration Melting model ($dV_S = -2.6\%$, $d_\rho = 0\%$). The square marks the true input parameters, and the star indicates the best-fit solution. Comparing these elongated valleys to the well-defined minima in the joint inversion (Main Text, Fig. 6) demonstrates the necessity of combining SS and PP data to resolve the density–velocity ambiguity.

Figure S9. Assessment of signal coherency in non-curvelet filtered Pacific data. Deconvolved receiver functions and vespagrams for the Pacific data set prior to the application of curvelet denoising. (a, c) SS results: (a) receiver function gather and (c) slowness-time vespagram. (b, d) PP results: (b) receiver function gather and (d) slowness-time vespagram. Compared to the filtered results in the main text (Fig. 11), the S800S phase is not resolvable in the vespagram (c); although intermittent energy is visible in the gather (a) near the expected arrival time, the phase coherence is degraded by noise, leading to destructive interference during stacking. This confirms that the coherent 800-km signal observed in the main text is revealed by, but not created by, the curvelet denoising process.

Figure S10. 2-D slowness grid search of the S800S arrival in the Hawaii region. Normalized stack energy is plotted as a function of radial and transverse slowness deviation relative to the main SS phase. The cross indicates the origin (0, 0), corresponding to the exact arrival angle of the main SS reference phase. The asterisk marks the theoretical 1-D PREM predicted arrival for the S800S phase at a radial slowness deviation of $-0.55\ \mathrm{s\,deg^{-1}}$. The observed peak energy is closely centered at a transverse slowness of $0.00\ \mathrm{s\,deg^{-1}}$, indicating the signal originates from an in-plane structure and ruling out out-of-plane scattering.

Figure S11. Bootstrap resampling analysis of the S800S signal in the NoMelt region. This analysis corresponds to the data presented in Fig. 11. The solid line represents the mean stacked amplitude of the data, while the shaded region indicates the 95% confidence interval derived from 1000 bootstrap iterations. The dashed line denotes zero amplitude. Crucially, the lower bound of the 95% confidence interval remains strictly positive during the S800S arrival. This confirms that the faint S800S reflection observed in the NoMelt region is statistically significant and a robust feature of the data set, ruling out the possibility of a spurious alignment of background noise.

Figure S12. Sensitivity analysis of the grid search inversion to incidence angle and distance-dependent stacking. (a) Theoretical reflection coefficients (R_{SS}) calculated for individual 1° epicentral distance bins (black squares) based on the best-fit model for the target region. The triangle denotes the reflection coefficient evaluated at the mean ray parameter ($p \approx 8.5$ s/$^\circ$) used in the primary inversion. The dashed line represents the mean of all distance-dependent models (the 'Forward-Modelled Stack'). The mean of the individual models is nearly identical to the model evaluated at the mean distance. (b, c) 1-D misfit profiles for (b) shear velocity contrast (δV_S) and (c) density contrast (δ_ρ). The solid curves represent the misfit calculated using a single averaged ray parameter, while the dashed curves represent the misfit calculated by forward-modelling and averaging all distance bins independently. The alignment of the minima (at $\delta V_S = 4\%$ and $\delta_\rho = 0\%$) demonstrates that the inversion results are robust.

Please note: Oxford University Press are not responsible for the content or functionality of any supporting materials supplied by the authors. Any queries (other than missing material) should be directed to the corresponding author for the article.

DATA AVAILABILITY

All seismic data used in this study can be obtained from the IRIS Data Management Center (https://ds.iris.edu/ds). Data and codes used for this work may be made available upon request.

REFERENCES

Aki, K. & Richards, P.G., 2002. *Quantitative Seismology,* University Science Books, Sausalito, CA.

Allègre, C.J. & Turcotte, D.L., 1986. Implications of a two-component marble-cake mantle, *Nature,* **323**(6084), 123–127.

Ballmer, M.D., Houser, C., Hernlund, J.W., Wentzcovitch, R.M. & Hirose, K., 2017. Persistence of strong silica-enriched domains in the Earth's lower mantle, *Nat. Geosci.,* **10**(3), 236–240.

Ballmer, M.D., Schmerr, N.C., Nakagawa, T. & Ritsema, J., 2015. Compositional mantle layering revealed by slab stagnation at 1000-km depth, *Sci. Adv.,* **1**(11), e1500815.

Bentham, H.L.M. & Rost, S., 2014. Scattering beneath Western Pacific subduction zones: evidence for oceanic crust in the mid-mantle, *Geophys. J. Int.,* **197**(3), 1627–1641.

Bercovici, D. & Karato, S.-I., 2003. Whole-mantle convection and the transition-zone water filter, *Nature,* **425**(6953), 39–44.

Bissig, F., Khan, A. & Giardini, D., 2022. Joint inversion of PP and SS precursor waveforms and Rayleigh wave phase velocities for global mantle transition zone structure, *Geophys. J. Int.,* **233**(1), 316–337.

Candes, E., Demanet, L., Donoho, D. & Ying, L., 2006. Fast discrete curvelet transforms, *Multiscale Model. Sim.,* **5**(3), 861–899.

Carr, S.A., Olugboji, T., Park, J. & Karato, S.-I., 2025. High-resolution mapping of North America suggests numerous low-velocity zones above and below the mantle transition zone, *Tectonophysics,* **908,** 230 775.

Chung, D. & Buessem, W., 1968. The Voigt-Reuss-Hill (VRH) approximation and the elastic moduli of polycrystalline ZnO, TiO2 (Rutile), and α-Al2O3, *J. Appl. Phys.,* **39**(6), 2777–2782.

Connolly, J.A., 2005. Computation of phase equilibria by linear programming: a tool for geodynamic modeling and its application to subduction zone decarbonation, *Earth planet. Sci. Lett.,* **236**(1–2), 524–541.

Cui, C., Lei, W., Liu, Q., Peter, D., Bozdağ, E., Tromp, J. & Pugmire, D., 2024. GLAD-M35: a joint P and S global tomographic model with uncertainty quantification, *Geophys. J. Int.,* **239**(1), 478–502.

Deuss, A., 2009. Global observations of mantle discontinuities using SS and PP precursors, *Surv. Geophys.,* **30**(4–5), 301–326.

Deuss, A., Redfern, S.A.T., Chambers, K. & Woodhouse, J.H., 2006. The nature of the 660-kilometer discontinuity in Earth's mantle from global seismic observations of PP precursors, *Science,* **311**(5758), 198–201.

Dziewonski, A.M. & Anderson, D.L., 1981. Preliminary reference Earth model, *Phys. Earth planet. Inter.,* **25**(4), 297–356.

Fei, H., 2021. Water content of the dehydration melting layer in the topmost lower mantle, *Geophys. Res. Lett.,* **48**(1), e2020GL090973.

Frazer, W.D. & Park, J., 2021. Seismic evidence of mid-mantle water transport beneath the Yellowstone regio, *Geophys. Res. Lett.,* **48**(20).

Frazer, W.D. & Park, J., 2023. High-resolution mid-mantle imaging with multiple-taper SS-precursor estimates, *Geophys. J. Int.,* **233**(2), 1356–1371.

Frazer, W.D. & Park, J., 2024. No globally detectable seismic interfaces within Earth's mantle transition zone: evidence for basalt enrichment, *Earth planet. Sci. Lett.,* **641**(118838), 118 838.

Fukao, Y. & Obayashi, M., 2013. Subducted slabs stagnant above, penetrating through, and trapped below the 660 km discontinuity, *J. Geophys. Res.: Solid Earth,* **118**(11), 5920–5938.

Goes, S., 2002. Thermal structure of the North American uppermost mantle inferred from seismic tomography, *J. geophys. Res.,* **107**(B3).

Goes, S., Yu, C., Ballmer, M.D., Yan, J. & van der Hilst, R.D., 2022. Compositional heterogeneity in the mantle transition zone, *Nat. Rev. Earth Environ.,* **3**(8), 533–550.

Grand, S.P., 2002. Mantle shear–wave tomography and the fate of subducted slabs, *Philos. T. R. Soc. Lond. Ser. A: Math. Phys. Eng. Sci.,* **360**(1800), 2475–2491.

Gu, Y.J. & Sacchi, M., 2009. Radon transform methods and their applications in mapping mantle reflectivity structure, *Surv. Geophys.,* **30**(4), 327–354.

Helffrich, G., 2006. Extended-time multitaper frequency domain cross-correlation receiver-function estimation, *Bull. seism. Soc. Am.,* **96**(1), 344–347.

Huang, Q., Schmerr, N., Waszek, L. & Beghein, C., 2019. Constraints on seismic anisotropy in the mantle transition zone from long-period SS precursors, *J. Geophys. Res.: Solid Earth,* **124**(7), 6779–6800.

Ishii, T., Miyajima, N., Criniti, G., Hu, Q., Glazyrin, K. & Katsura, T., 2022. High pressure-temperature phase relations of basaltic crust up to mid-mantle conditions, *Earth planet. Sci. Lett.,* **584**(117472), 117 472.

Jenkins, J., Deuss, A. & Cottaar, S., 2017. Converted phases from sharp 1000 km depth mid-mantle heterogeneity beneath Western Europe, *Earth planet. Sci. Lett.,* **459,** 196–207.

Karato, S.-I., 2014. Does partial melting explain geophysical anomalies?, *Phys. Earth planet. Inter.,* **228,** 300–306.

Karato, S.-I., Karki, B. & Park, J., 2020. Deep mantle melting, global water circulation and its implications for the stability of the ocean mass, *Prog. Earth Planet. Sci.,* **7**(1), 76.

Lessing, S., Thomas, C., Saki, M., Schmerr, N. & Vanacore, E., 2015. On the difficulties of detecting PP precursors, *Geophys. J. Int.,* **201**(3), 1666–1681.

Liu, Z., Park, J. & Karato, S.-I., 2018. Seismic evidence for water transport out of the mantle transition zone beneath the European Alps, *Earth planet. Sci. Lett.,* **482,** 93–104.

Lord, O.T., 2022. Hydrous silicate melts and the deep mantle H2O cycle, *Sciences,* **34,** 629–653.

Marquardt, H. & Miyagi, L., 2015. Slab stagnation in the shallow lower mantle linked to an increase in mantle viscosity, *Nat. Geosci.,* **8**(4), 311–314.

Murakami, M., Khan, A., Sossi, P.A., Ballmer, M.D. & Saha, P., 2024. The composition of Earth's lower mantle, *Annu. Rev. Earth Planet. Sci.,* **52**(1), 605–638.

Naghizadeh, M., 2012. Seismic data interpolation and denoising in the frequency-wavenumber domain, *Geophysics,* **77**(2), V71–V80.

Nakagawa, T., Tackley, P.J., Deschamps, F. & Connolly, J.A., 2010. The influence of MORB and harzburgite composition on thermo-chemical mantle convection in a 3-D spherical shell with self-consistently calculated mineral physics, *Earth planet. Sci. Lett.,* **296**(3–4), 403–412.

Nissen-Meyer, T., Basini, P. & Tromp, J., 2011. Forward and adjoint simulations of seismic wave propagation on fully unstructured hexahedral meshes, *Geophys. J,* **186**(2), 721–739.

Olugboji, T., Zhang, Z., Carr, S., Ekmekci, C. & Cetin, M., 2023. On the detection of upper mantle discontinuities with radon-transformed receiver functions (CRISP-RF), *Geophys. J. Int.,* **236**(2), 748–763.

Park,, J. & Levin, V., 2000. Receiver functions from multiple-taper spectral correlation estimates, *Bull. Seismol. Soc. Am.,* **90**(6), 1507–1520.

Park, J. & Levin, V., 2016. Statistics and frequency-domain moveout for multiple-taper receiver functions, *Geophys. J. Int.,* **207**(1), 512–527.

Ritsema, J., Deuss, A., van Heijst, H.J. & Woodhouse, J.H., 2011. S40RTS: a degree-40 shear-velocity model for the mantle from new Rayleigh wave dispersion, teleseismic traveltime and normal-mode splitting function measurements, *Geophys. J. Int.,* **184**(3), 1223–1236.

Ritsema, J., Xu, W., Stixrude, L. & Lithgow-Bertelloni, C., 2009. Estimates of the transition zone temperature in a mechanically mixed upper mantle, *Earth planet. Sci. Lett.,* **277**(1), 244–252.

Rudolph, M.L., Lekić, V. & Lithgow-Bertelloni, C., 2015. Viscosity jump in Earth's mid-mantle, *Science,* **350**(6266), 1349–1352.

Schmandt, B., Jacobsen, S.D., Becker, T.W., Liu, Z. & Dueker, K.G., 2014. Dehydration melting at the top of the lower mantle, *Science,* **344**(6189), 1265–1268.

Schneider, S., Thomas, C., Dokht, R.M., Gu, Y.J. & Chen, Y., 2018. Improvement of coda phase detectability and reconstruction of global seismic data using frequency–wavenumber methods, *Geophys. J. Int.,* **212**(2), 1288–1301.

Shearer, P.M. & Flanagan, M.P., 1999. Seismic velocity and density jumps across the 410- and 660-kilometer discontinuities, *Science,* **285**(5433), 1545–1548.

Shen, Y., Wolfe, C.J. & Solomon, S.C., 2003. Seismological evidence for a mid-mantle discontinuity beneath Hawaii and Iceland, *Earth planet. Sci. Lett.,* **214**(1), 143–151.

Stixrude, L. & Lithgow-Bertelloni, C., 2012. Geophysics of Chemical Heterogeneity in the Mantle, *Annu. Rev. Earth Planet. Sci.,* **40**, 569–595.

Tauzin, B., Debayle, E. & Wittlinger, G., 2010. Seismic evidence for a global low-velocity layer within the Earth's upper mantle, *Nat. Geosci.,* **3**(10), 718–721.

Tauzin, B., Waszek, L., Ballmer, M.D., Afonso, J.C. & Bodin, T., 2022. Basaltic reservoirs in the Earth's mantle transition zone, *Proc. Natl. Acad. Sci. USA,* **119**(48), e2209399119.

van Keken, P.E., Hauri, E.H. & Ballentine, C.J., 2002. Mantle mixing: the generation, preservation, and destruction of chemical heterogeneity, *Annu. Rev. Earth Planet. Sci.,* **30**(1), 493–525.

Wang, J., Lekić, V., Schmerr, N.C., Gu, Y.J., Guo, Y. & Lin, R., 2024. Mesozoic intraoceanic subduction shaped the lower mantle beneath the East Pacific Rise, *Sci. Adv.,* **10**(39), eado1219.

Waszek, L., Schmerr, N.C. & Ballmer, M.D., 2018. Global observations of reflectors in the mid-mantle with implications for mantle structure and dynamics, *Nat. Commun.,* **9**(1), 385.

Waszek, L., Tauzin, B., Schmerr, N.C., Ballmer, M.D. & Afonso, J.C., 2021. A poorly mixed mantle transition zone and its thermal state inferred from seismic waves, *Nat. Geosci.,* **14**(12), 949–955.

Wookey, J., Kendall, J.-M. & Barruol, G., 2002. Mid-mantle deformation inferred from seismic anisotropy, *Nature,* **415**(6873), 777–780.

Xu, W., Lithgow-Bertelloni, C., Stixrude, L. & Ritsema, J., 2008. The effect of bulk composition and temperature on mantle seismic structure, *Earth planet. Sci. Lett.,* **275**(1), 70–79.

Yan, J., Ballmer, M.D. & Tackley, P.J., 2020. The evolution and distribution of recycled oceanic crust in the Earth's mantle: Insight from geodynamic models, *Earth planet. Sci. Lett.,* **537**(116171), 116 171.

Yoshino, T., Nishihara, Y. & Karato, S.-I., 2007. Complete wetting of olivine grain boundaries by a hydrous melt near the mantle transition zone, *Earth planet. Sci. Lett.,* **256**(3–4), 466–472.

Yu, C., Day, E.A., de Hoop, M.V., Campillo, M. & van Der Hilst, R.D., 2017. Mapping mantle transition zone discontinuities beneath the Central Pacific with array processing of SS precursors, *J. Geophys. Res.: Solid Earth,* **122**(12), 10–364.

Yu, C., Goes, S., Day, E.A. & van der Hilst, R.D., 2023. Seismic evidence for global basalt accumulation in the mantle transition zone, *Sci. Adv.,* **9**(22), eadg0095.

Zhang, J. & Langston, C.A., 2020. Separating the scattered wavefield from teleseismic P using curvelets on the long beach array data set, *Geophys. J. Int.,* **220**(2), 1112–1127.

Zhang, Z., Irving, J.C.E., Simons, F.J. & Alkhalifah, T., 2023. Seismic evidence for a 1000 km mantle discontinuity under the Pacific, *Nat. Commun.,* **14**(1), 1714.

Zheng, Z., Ventosa, S. & Romanowicz, B., 2015. High resolution upper mantle discontinuity images across the Pacific Ocean from SS precursors using local slant stack filters, *Geophys. J. Int.,* **202**(1), 175–189.

Zhou, H.-W., 2014. *Practical Seismic Data Analysis* Cambridge University Press.